Propagation of sharp wave-ripple activity in the mouse hippocampal CA3 subfield *in vitro*

Natalie Schieferstein[1,2] , Ana del Toro[1,2], Roberta Evangelista[1,2] , Barbara Imbrosci[3,4],
Aarti Swaminathan[4] , Dietmar Schmitz[2,3,4,5,6], Nikolaus Maier[4] and Richard Kempter[1,2,6]

[1]*Department of Biology, Institute for Theoretical Biology, Humboldt-Universität zu Berlin, Berlin, Germany*
[2]*Bernstein Center for Computational Neuroscience Berlin, Berlin, Germany*
[3]*German Center for Neurodegenerative Diseases (DZNE) Berlin, Berlin, Germany*
[4]*Charité–Universitätsmedizin Berlin, Corporate Member of Freie Universität Berlin and Humboldt-Universität zu Berlin, and Berlin Institute of Health, Berlin, Germany*
[5]*NeuroCure Cluster of Excellence, Berlin, Germany*
[6]*Einstein Center for Neurosciences (ECN) Berlin, Berlin, Germany*

Handling Editors: Katalin Toth & Jean-Claude Béïque

The peer review history is available in the Supporting Information section of this article (https://doi.org/10.1113/JP285671#support-information-section).

Abstract Sharp wave-ripple complexes (SPW-Rs) are spontaneous oscillatory events that characterize hippocampal activity during resting periods and slow-wave sleep. SPW-Rs are related

N. Schieferstein, A. del Toro and R. Evangelista are co-first authors.
N. Maier and R. Kempter are co-last authors.

to memory consolidation – the process during which newly acquired memories are transformed into long-lasting memory traces. To test the involvement of SPW-Rs in this process, it is crucial to understand how SPW-Rs originate and propagate throughout the hippocampus. SPW-Rs can originate in CA3, and they typically spread from CA3 to CA1, but little is known about their formation within CA3. To investigate the generation and propagation of SPW-Rs in CA3, we recorded from mouse hippocampal slices using multi-electrode arrays and patch-clamp electrodes. We characterized extracellular and intracellular correlates of SPW-Rs and quantified their propagation along the pyramidal cell layer of CA3. We found that a hippocampal slice can be described by a speed and a direction of propagation of SPW-Rs. The preferred propagation direction was from CA3c (the subfield closer to the dentate gyrus) toward CA3a (the subfield at the boundary to CA2). In patch-clamp recordings from CA3 pyramidal neurons, propagation was estimated separately for excitatory and inhibitory currents associated with SPW-Rs. We found that propagation speed and direction of excitatory and inhibitory currents were correlated. The magnitude of the speed of propagation of SPW-Rs within CA3 was consistent with the speed of propagation of action potentials in axons of CA3 principal cells.
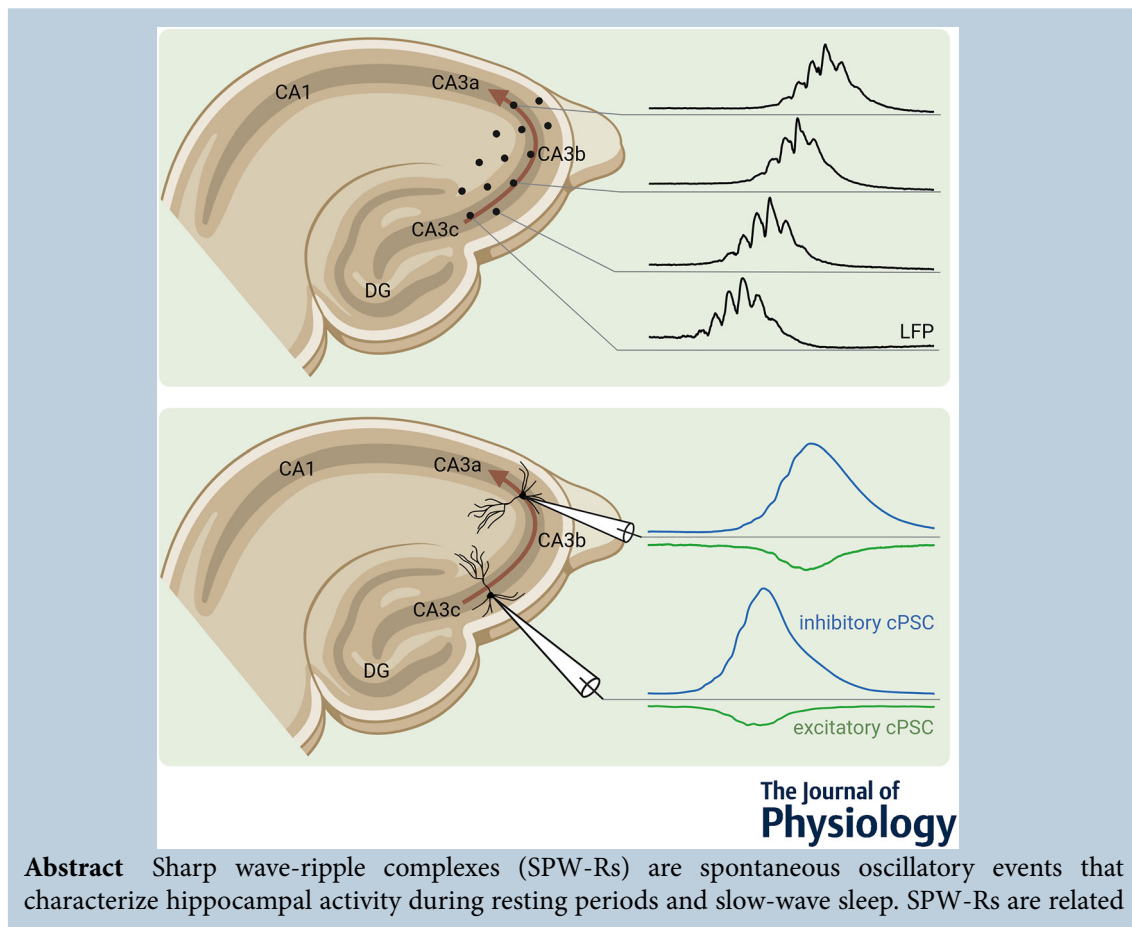
Corresponding authors N. Maier: Charité–Universitätsmedizin Berlin, Corporate Member of Freie Universität Berlin and Humboldt-Universität zu Berlin, and Berlin Institute of Health, Berlin, Germany. Email: nikolaus.maier@charite.de

R. Kempter: Department of Biology, Institute for Theoretical Biology, Humboldt-Universität zu Berlin, Berlin, Germany. Email: r.kempter@biologie.hu-berlin.de

Abstract figure legend Hippocampal sharp wave-ripple activity constitutes brief, localized depolarization events that propagate along the *stratum pyramidale* of the hippocampal subfield CA3. This study investigates the propagation of sharp waves *in vitro*. Both local field potential (LFP) and voltage-clamp recordings of sharp wave-associated excitatory or inhibitory compound postsynaptic currents (cPSCs) suggest a predominant direction of propagation from subfield CA3c toward CA3a.

Key points

- Hippocampal sharp waves are considered important for memory consolidation; therefore, it is of interest to understand the mechanisms of their generation and propagation.
- Here, we used two different approaches to study the propagation of sharp waves in mouse CA3 *in vitro*: multi-electrode arrays and multiple single-cell recordings.
- We find a preferred direction of propagation of sharp waves from CA3c toward CA3a – both in the local field potential and in sharp wave-associated excitatory and inhibitory synaptic activity.
- The speed of sharp wave propagation is consistent with the speed of action potential propagation along the axons of CA3 pyramidal neurons.
- These new insights into the dynamics of sharp waves in the CA3 network will inform future experiments and theoretical models of sharp-wave generation mechanisms.

Introduction

The hippocampus is critical for systems memory consolidation, and hippocampal ripples – often in conjunction with local field potential (LFP) sharp waves (sharp wave ripple complexes, SPW-Rs) – are thought to be a mechanism for the transfer of memories from the hippocampus to the neocortex (Buzsáki, 2015; Jadhav et al., 2016). During SPW-Rs, hippocampal ensembles are reactivated (Kudrimoti et al., 1999; Lee & Wilson, 2002; Nádasdy et al., 1999; Wilson & McNaughton, 1994). Furthermore, sharp wave-associated ripples, and in particular the firing of neurons reactivated during SPW-Rs, have been demonstrated to contribute to synaptic plasticity (King et al., 1999; Sadowski et al., 2016). The disruption of SPW-Rs impairs memory formation (Ego-Stengel & Wilson, 2010; Girardeau et al., 2009), whereas the experimental prolongation of SPW-Rs enhances memory (Fernández-Ruiz et al., 2019).

SPW-Rs are short (typically 50−100 ms) episodes of coordinated network activity arising mainly in the hippocampal areas CA3 (Buzsáki, 1989; Ellender et al.,

2010) and CA2 (Oliva et al., 2016), but can also be generated in CA1 (Maier et al., 2003) or the subiculum (Imbrosci et al., 2021). SPW-R activity patterns dominate in the hippocampus during slow-wave sleep, quiet wakefulness and consummatory behaviours (Buzsáki, 1986; Chrobak & Buzsáki, 1996). In a SPW-R episode, the LFP shows a transient low-frequency (<50 Hz) 'sharp wave' (SPW) deflection, which represents synchronous dendritic synaptic input (Buzsáki et al., 1983; Evangelista et al., 2020; Sullivan et al., 2011). The SPW is overlaid by high-frequency (≈150 Hz) 'ripple' oscillations, which are thought to be due to synchronized synaptic activity in local networks (Buzsáki et al., 1992; Donoso et al., 2018; English et al., 2014; Stark et al., 2014).

The CA3 region is involved in the generation of SPW-Rs (Buzsáki, 1989; Ellender et al., 2010), but CA3 is inhomogeneous with respect to recurrent collaterals, output pathways and the induction of SPW-Rs (Csicsvari et al., 2000). The CA3 region can be subdivided into a 'distal' CA3a subregion adjacent to the CA2 region, a subregion CA3b and a 'proximal' subregion CA3c adjacent to the dentate hilus (Lorente de Nò, 1934). Pyramidal cells in CA3a and distal CA3b exhibit recurrent collaterals that are mostly confined to CA3, whereas pyramidal cells in proximal CA3b and CA3c predominantly project to the CA1 region (Ishizuka et al., 1990; Li et al., 1994), which might influence the site(s) of SPW genesis.

To determine the mechanisms of how SPW-Rs are generated in CA3, we investigated at which locations they first appear and how they propagate through the CA3 network. We show here that in acute mouse hippocampal slices SPW-Rs preferentially propagate in the direction from CA3c toward CA3a with a speed that is consistent with action potential propagation.

Materials and methods

Ethics approval

Animal maintenance and experiments followed institutional guidelines, the guidelines of the Berlin state (T0100/03), and the European Union (EU) Council Directive 2010/63/EU on the protection of animals used for experimental and other scientific purposes.

Subjects

Inbred mice used in this study were obtained from the Experimental Medicine Research Facilities (FEM) of Charité–Universitätsmedizin Berlin and were housed with *ad libitum* access to food and water. A total of 29 male C57BL/6N mice, aged 3 to 9 weeks, were analysed.

Slice preparation

Following isoflurane anaesthesia, mice were decapitated, and the brain was removed and placed in an ice-cold, sucrose-based artificial cerebrospinal fluid that was saturated with carbogen (95% vol/vol O_2, 5% vol/vol CO_2) and contained (in mM): 87 NaCl, 26 $NaHCO_3$, 50 saccharose/sucrose, 10 glucose, 2.5 KCl, 1.25 NaH_2PO_4, 0.5 $CaCl_2$, 3 $MgCl_2$. After ≈5 min of recovery, horizontal slices ($350-400$ μm thick) were cut using a vibratome (VT1200, Leica Biosystems, Wetzlar, Germany) starting from the ventral pole of the hippocampus. Slices used in this study are from the ventral to middle portion of the hippocampus, and *post hoc* alignment of their images with anatomical references confirms their position in the range of $[-2.80, -3.76]$ mm with respect to bregma, corresponding to figures 156 to 146 in Franklin & Paxinos (2007). Subsequently, the slices were stored in a holding chamber for recovery (temperature $33-35°C$) for at least 1 h, constantly perfused with ACSF, containing (in mM): 119 NaCl, 26 $NaHCO_3$, 10 glucose, 2.5 KCl, 1.25 NaH_2PO_4, 2.5 $CaCl_2$, 1.3 $MgCl_2$, and kept at the interface between ACSF and humidified carbogen.

It should be noted that the slicing procedure in ice-cold ACSF can induce a transient loss of spines (Kirov et al., 2004); spines were shown to re-emerge within 30 min, and spine and synapse number reached a plateau within 2 h. Our experiments were performed within $2-7$ h after slicing.

Natalie Schieferstein received her PhD from Humboldt-Universität zu Berlin where she studied the dynamics of hippocampal ripple oscillations in inhibitory network models. She is now a postdoctoral researcher at Universität Bonn. Her research interests revolve around the dynamics of spiking neural networks and their implications for information processing and learning. **Ana del Toro** obtained an MSc in Computational Neuroscience from the Bernstein Centre for Computational Neuroscience Berlin (BCCNB). This background in programming, modelling and statistical analysis enabled her to start a career as a data analyst at a company in Berlin. **Roberta Evangelista** obtained an MSc in Computational Neuroscience from the BCCNB and started this project in her Master thesis. She completed a PhD at Humboldt-Universität zu Berlin developing theoretical and computational models of hippocampal rhythms. All of this was crucial to shaping her interest in data science. She is now working at a not-for-profit organization based in Switzerland.
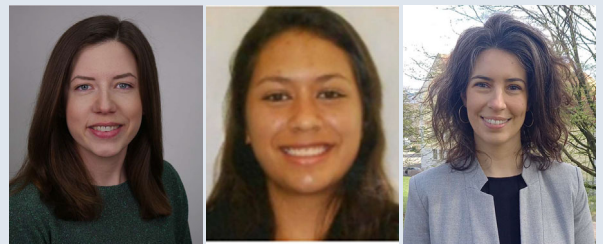
In vitro-model of SPW-Rs

In this experimental system, SPW-Rs arise spontaneously in slices bathed in standard ACSF. This implies that neither pharmacological nor electrical stimulation is required for their induction (Çalışkan et al., 2023; Chiovini et al., 2014; El Oussini et al., 2023; Hájos et al., 2013; Jiang et al., 2018; Kanak et al., 2013; Kubota et al., 2003; Maier et al., 2002, 2003; Moradi-Chameh et al., 2014; Norimoto et al., 2018; Papatheodoropoulos & Kostopoulos, 2002; Zarnadze et al., 2016). It should be noted that patterns of network activity can also be *induced* in hippocampal slices; for example, following blockade of $GABA_A$ receptors or increase in extracellular K^+ or decrease in Mg^{2+}. However, these patterns are thought to have characteristics of pathological network activity and therefore serve as models for epileptiform or inter-ictal events (Karlócai et al., 2014; Khazipov et al., 2004; Schneiderman, 1986; Wong & Traub, 1983).

Electrophysiology

MEA recordings. The slices were transferred to a perforated multi-electrode array (MEA) system (USB-MEA32STIM4, Multi Channel Systems MCS GmbH, Reutlingen, Germany), where they were placed on the central electrode-loaded region of the membrane (Fig. 1*A*). Slices were perfused at ≈1 ml/min with carbogenated ACSF, the temperature of which was maintained at ≈34°C in the recording chamber. A second chamber below the membrane was pressurized to a slight vacuum of ≈18–20 mbar, which exerted negative pressure on the slice via the perforation (Fig. 1*Ab*) that resulted in (1) improved contact between the slice and the electrodes and (2) increased flow of ACSF from the recording chamber through the slice. The perforation of MEA membranes has been demonstrated to improve tissue oxygenation and signal quality (Egert et al., 2005). The perforated MEA systems used for this project have 32 recording channels, organized in [8, 8, 8, 8] or [10, 12, 10] configurations; see, for example, Fig. 1*Ab–c*. The electrode diameter is 30 μm, and the interelectrode distance varies, depending on the layout, from 90 to 150 μm. The slices were positioned to preferentially record LFPs from the pyramidal cell layer in area CA3. After a recovery period (≈5−10 min), data were acquired in two recordings of approximately 300 s each (sampling rate 20 kHz), using the MC Rack software (Multi Channel Systems). In all recorded slices, SPW-R events occurred spontaneously, and their quantification and further analysis were performed offline. In total, we analysed data from 25 slices taken from eight animals. In six recordings, slices were further stored for histological analysis.

Combined LFP/whole-cell recordings. Recordings were made in standard ACSF at 31−32°C in a submerged-type recording chamber perfused at 5−6 ml/min (Maier et al., 2009). For LFP recordings, glass microelectrodes (tip opening ≈5−10 μm; 0.2−0.3 MΩ) were filled with ACSF. Whole-cell voltage-clamp recordings were conducted near the inhibitory reversal potential (≈−60 mV) or the excitatory reversal potential (≈+6 mV) using glass electrodes (2−5 MΩ) filled with cesium-based intra-cellular solution containing (in mM): 117.5 gluconic acid, 8 NaCl, 10 TEA, 10 HEPES, 0.2 EGTA, 5 QX-314, 2.5 CsCl, 0.3 Na_2GTP and 4 MgATP, 5.4 biocytin (0.2%); pH adjusted to 7.4 with CsOH. Signals were amplified 1000× (for LFPs) or 5× (for whole-cell data) using Multiclamp 700A or B amplifiers (Molecular Devices, San Jose, CA, USA), respectively. Data were low-pass filtered at 3−4 kHz (Bessel filter) and digitized at 10−20 kHz with 16-bit resolution using an A/D converter (BNC2090 board, National Instruments, Austin, TX, USA; or Axon Digidata 1550A, Molecular Devices). Igor Pro (Wave-metrics, Lake Oswego, OR, USA) or pClamp (Molecular Devices) were used for data storage. The series resistance R_s was measured by applying a voltage pulse of −4 mV amplitude and 50 ms duration at the beginning of each sweep; recordings were rejected if R_s exceeded 25 MΩ or varied >30%. No compensation of R_s was applied. Further, these Cs-based recordings were rejected if the holding current I_{hold} required to keep the cells at $V_{hold} = -60$ mV exceeded −400 pA. In total, we analysed data from 32 slices taken from 21 mice. Slices were routinely stored in 4% paraformaldehyde (PFA) for immunohistochemical processing (see below, section *Stainings and anatomical identification of recorded cells*).

Data analysis: MEA recordings

Identification of recording positions. During the experiments, photographs of the recorded slices were taken for later assignment of MEA channels to their anatomical positions (see Fig. 1). We discarded slices in which the structure of the cornu ammonis (CA) was not clearly visible in the photograph.

To identify and denote the subsections of the CA3 field, we follow the terminology of Lorente de Nò (1934), who divided CA3 into three parts: CA3a, CA3b and CA3c; see, for example, Fig. 1*Ac*. Because the boundaries between these subsections are not clearly defined and this classification is rather crude, we standardized the positions of the MEA recording electrodes in relation to the extent of CA3 rather than following the terminology of Lorente de Nò (1934). That is, the location within CA3 *stratum pyramidale* (*str. pyr.*) was quantified based on the extent of the CA3 pyramidal cell layer from its starting point in CA3c within the hilus (0%) to its ending
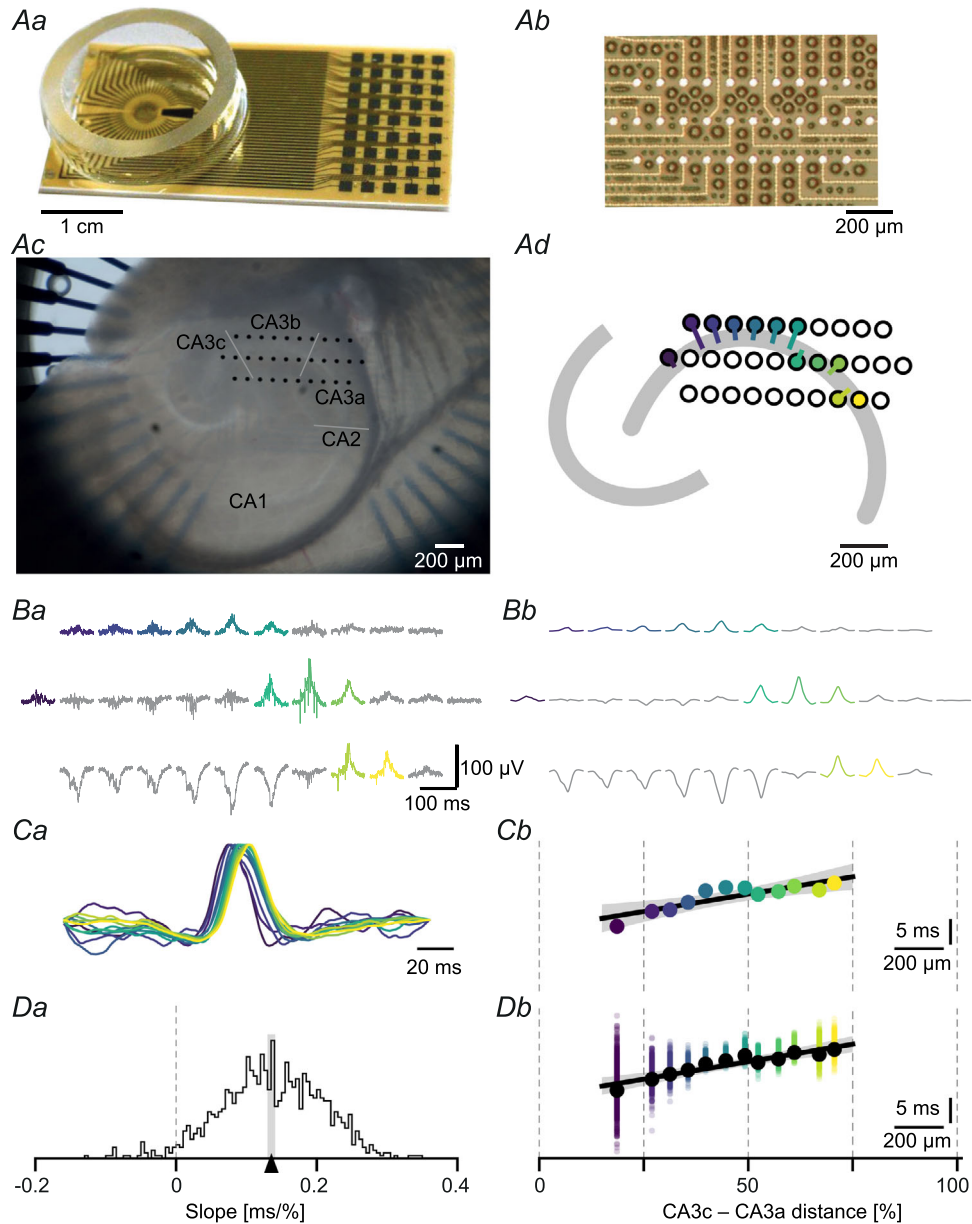
Figure 1. CA3 SPW-Rs in a multielectrode-array (MEA) recording *in vitro*

Aa, experimental system used in this study for MEA recordings. The slices were mounted on planar electrodes embedded in the membrane in the circular centre of the chamber and continuously superfused with ACSF. *Ab*, top view of the electrode array (white dots in three rows). The electrodes are embedded in a grid of perforation pores (visible as brownish rings) in the membrane, which improve the contact between tissue and electrodes and the oxygen supply through slight suction from below (see *Materials and methods*). Photograph and schematic courtesy of Multi Channel Systems, Reutlingen, Germany. *Ac*, photo of slice ID: 17 with 32 electrode positions (dots) indicated. Light grey solid lines indicate the approximate boundaries between CA3 subfields. *Ad*, sketch of MEA recording sites (circles) shown in (*Ac*) indicating channels of interest (coloured circles) and their projection (coloured lines) onto *str. pyr.* (larger curved grey band). Smaller curved grey band: granule cell layer. *Ba*, raw LFP traces from all 32 channels during a SPW-R event. Coloured traces indicate channels of interest marked in (*Ad*). *Bb*, filtered (5−40 Hz) LFP traces highlight the low-frequency SPW component. *Ca*, LFP traces from channels of interest shown in *Bb*, normalized to a common amplitude and overlaid for comparison. *Cb*, latencies of SPW arrival based on the LFP signals shown in (*Ca*) as a function of position along *str. pyr.* from CA3c to CA3a in %. Linear regression (black line) yields a positive propagation slope (0.1346 [0.06, 0.21] ms/%, r^2 = 0.75, 99% CI in brackets). *Da*, distribution of regression slopes for all SPW events measured in this slice. Triangle: mean regression slope (0.1354 ms/%); grey area: 99% bootstrap CI ([0.13, 0.14] ms/%). *Db*, latencies of SPW arrival as

a function of electrode position, shown for all SPW events (coloured dots). Linear regression (black line) over the average latencies (black dots) yields a positive propagation slope (0.1354 [0.09, 0.18] ms/%, r^2 = 0.89, 99% CI in brackets).

point in CA3a around the disappearance of the mossy fibre tract (100%). In detail, the total length of the curved *str. pyr.* was approximated by linear segments between 3 and 6 reference points within *str. pyr.* Then, the positions of MEA recording electrodes were extracted graphically from the slice photo. For MEA electrodes that were located outside *str. pyr.* we used the projection onto *str. pyr.* (points of minimal Euclidean distance); see Fig. 1*Ad*. The resulting one-dimensional coordinates were derived as the relative positions (in percent) of the projection points with respect to the total length of the curved *str. pyr.* from proximal CA3c (0%) to distal CA3a (100%).

LFP analysis. All acquired LFP data were inspected offline to check for artefacts, and each recording was further analysed independently using MATLAB (The MathWorks, Natick, MA, USA; R2013a, R2022a, R2022b) and Python 3 (Python Software Foundation). SPWs were detected as positive-going events in the low-pass filtered signal (5−40 Hz, first order Butterworth filter). MEA recording channels representing signals generated in the *str. pyr.* – usually displaying positive SPW amplitudes – were isolated as channels of interest (COIs), and the one with the largest SPW amplitude was taken as the reference channel. In the reference channel, the detection threshold for SPWs was chosen as the mean low-pass filtered LFP signal, plus 2−5 SDs, similar to procedures used before (Maier et al., 2009). In the remaining COIs, which all had lower SPW amplitudes, the detection threshold was lowered to 1−2.5 SDs above the mean. The proper choice of the detection threshold depended on the quality of the recordings and was confirmed by visual inspection. Windows of activity ±100 ms surrounding each SPW peak were cut out for further analysis. Only those SPW events that passed the detection threshold at all COIs entered the subsequent propagation analysis.

A very small fraction of events showed noisy traces, generally caused by air bubbles, dirt or technical issues; if the average baseline signal before or after a SPW event (first or last 50 ms in a SPW-event time window) was more than 3 SD above the overall event-free mean, the corresponding event was discarded as noisy and excluded from further analysis.

Sharp waves were characterized in terms of inter-event intervals, amplitude (maximum positive peak of the filtered LFP trace) and duration (time in which the 5−40 Hz filtered signal remained above the baseline value of 0 mV).

For the analysis of ripple frequency, the LFP signal was band-pass filtered in the ripple range (150−250 Hz, first order Butterworth). The ripple frequency was extracted as the inverse of the interval between the central and the adjacent peak in the auto-correlogram of the filtered signal. The calculation of the average ripple frequency (at a given COI) was restricted to SPW events with significant ripple modulation ('SPW-R events'). The significance of the ripple modulation was assessed by comparing the time-dependent root mean square (RMS) power of the filtered signal (square sliding window of 1.6 ms width) with a threshold value. The threshold value was defined as the mean +0.5 SD of the time-dependent RMS power, calculated over *all* SPW-event time windows (square sliding window of 2.5 ms width). For a given SPW event, only the time around the peak of the filtered signal with time-dependent RMS power *above* this threshold was considered a putative ripple interval (cf. Csicsvari et al., 1999b,a). To exclude brief increases in ripple power due to recording artefacts or noise, putative ripple intervals were discarded if their RMS power did not exceed the mean +0.2 SD of the time-dependent RMS power calculated across all event windows. The mean and SD of the ripple frequency were computed across only the accepted SPW-*R* events.

SPW and ripple properties were quantified separately for each COI. All SPW and ripple properties are reported in the *Results* in terms of mean and SD computed across the COI means of all slices.

Analysis of SPW propagation. The propagation of SPWs was assessed on a single-event basis, using the low-pass filtered LFP signals from all COIs. The shape of these SPW signals was comparable across all COIs. The SPW signal of each COI was cross-correlated with the signal at the reference channel. The cross-correlogram usually showed a distinct peak, the time lag of which was used as an estimate of the latency of SPW onset in the respective COI relative to the reference channel. SPW events with inferred onset latencies larger than 20 ms at any of the COIs were excluded from the analysis. The number of excluded events was small (one event in slice ID: 9, 12, 13, 19; two events in slice ID: 8; 14 events in slice ID: 4; 30 events in slice ID: 21; 50 events in slice ID: 23). For each accepted event, linear regression over the relative SPW onset latencies of all COIs provided a propagation slope (in ms/%). A non-zero slope indicates that a SPW event did not occur simultaneously at all COIs but propagated along the *str. pyr.* axis. For propagating SPW events, the inverse of the absolute value of the propagation slope can be taken as an estimate of propagation speed (%/ms or m/s when taking into account the length of *str. pyr.* in the respective slice).

A statistical analysis of SPW propagation was performed for every slice. Single-event propagation slopes were mostly unimodally distributed in all slices. The 99% confidence intervals (CI) for the mean propagation slope and median propagation speed were computed using the bias-corrected and accelerated bootstrap (100,000 resamples with replacement from the single-event propagation slopes; Ho et al., 2019). The significance of the mean propagation slope β (with respect to the null hypothesis $\beta = 0$) was assessed using a permutation test for the regression across the average SPW latencies measured at each of the COIs (two-sided *p*-value, $\alpha = 0.01$).

Data analysis: combined LFP/whole-cell recordings

Identification of recording positions. The positions of the pyramidal cell somata were extracted from histological images (see section *Stainings and anatomical identification of recorded cells*) and expressed as a one-dimensional coordinate with respect to the total length of the curved *str. pyr.* from CA3c (0%) to CA3a (100%) (see *Data analysis: MEA recordings*). The absolute distance between cells along the *str. pyr.* axis (in mm) was inferred by multiplying the difference in their relative position (in %) by the estimated total length of *str. pyr.* (in mm) in a given slice.

LFP analysis. Sharp waves were detected in the LFP signal as described above for the MEA data set. The SPW detection threshold was set to 2.5 SDs above the mean low-pass filtered LFP signal, and was confirmed by visual inspection (Maier et al., 2009). For the analysis of ripple frequency, the LFP signal was band-pass filtered in the ripple range (150−250 Hz, first order Butterworth). The ripple frequency was extracted as the inverse of the interval between the central and the adjacent peak in the auto-correlogram of the filtered signal. The average ripple frequency in a given slice was calculated across all SPW events without applying further threshold criteria.

All SPW and ripple properties are reported in the *Results* in terms of means and SDs computed across slices.

Propagation analysis of SPW-associated synaptic activity. For each SPW event and each cell, the SPW-associated compound excitatory or inhibitory postsynaptic current (cEPSC or cIPSC) was extracted in a time window of 600 ms centred on the SPW peak in the LFP. To isolate the slower component reflecting local SPW-related synaptic activity, all cEPSCs and cIPSCs were bandpass-filtered (0.1−80 Hz).

The propagation of SPW-associated synaptic activity was assessed on a single-event basis. Because (normalized) compound postsynaptic currents (cPSCs) measured in different cells can have very different time courses, we estimated their propagation not by cross-correlating the entire time series (see *Data analysis: MEA recordings*) but by comparing the 'onset times' of corresponding cPSCs in different cells. To determine the onset time (t_0) of a cPSC, the rising phase before its peak (at time t_{peak}) was fitted with a linear threshold function ($\sim m(t − t_0)\Theta(t − t_0) + b$) with the fit parameters slope m, baseline b and onset time t_0.

In most slices, two cells were recorded simultaneously. In that case, the difference between the onset times of the respective cPSCs was taken as an estimate of SPW propagation delay. A propagation slope (in ms/% or s/m) was inferred by dividing the delay by the distance between the somata of the recorded cells along the *str. pyr.* axis. In cases in which three cells were recorded simultaneously, a linear regression was performed over the respective onset times to infer the propagation slope. Propagation speed (in %/ms or m/s) was inferred by taking the inverse of the absolute propagation slope.

We note that this analysis of the propagation of SPW-associated cPSCs, which we measured using voltage-clamp recordings, is largely unaffected by fluctuations in the reversal potentials. The reversal potentials may fluctuate during the span of a SPW-R event due to voltage-dependent membrane conductances. The composition of the intracellular solution used, containing TEA, Cs^+ and QX-314, substantially reduces K^+-based conductances and Na^+-driven spiking activities (Monier et al., 2008; Simonnet et al., 2021). Furthermore, the above-described read-out parameter ('onset time') is robust against variations in the amplitude of the cPSCs.

SPW-associated cPSCs in single cells were excluded from further analysis if at least one of the following criteria was met: (1) cPSCs had a polarity that did not match the direction of the driving force at the particular holding potential; (2) the recording was too noisy (peak in cPSC was smaller than the baseline current plus 2 SD); (3) the threshold-linear fit of the rise time failed (mean squared error larger than 0.1 pA^2); or (4) the rise time ($t_{peak} − t_0$) was longer than 30 ms. For SPW events with accepted cPSCs in all cells (7862/9603 events, *i.e.* 81.87%), the propagation delay was determined as described above. Three recording sessions (two or three cells recorded simultaneously at the same holding potential) were excluded from analysis, because they contained less than 25 admissible SPW events (slice ID: 19, cIPSC recording; slice ID: 21, both cIPSC and cEPSC recordings). In slices ID: 9, 12 and *i.e.*17, only cIPSCs were recorded.

A statistical analysis of the propagation of SPW-related activity was performed for every slice. Propagation in a given slice was quantified by the *median* propagation slope, since the distributions of single-event slopes contained outliers and were at times skewed. The significance of the median propagation slope β (with

respect to the null hypothesis $\beta = 0$) was assessed using a two-sided one-sample Wilcoxon's signed-rank test ($\alpha = 0.01$). The 99% CIs for the median slope and median speed were obtained with the bias-corrected and accelerated bootstrap (100,000 resamples with replacement, Ho et al., 2019).

Stainings and anatomical identification of recorded cells

Cells were routinely filled with 0.2% biocytin and, after recordings, slices were placed in 4% PFA for overnight fixation and then stored at 4°C in 0.1 м phosphate-buffered saline (PBS) containing 0.1% sodium azide. For immunostainings, slices were washed 3× with 0.1 м PBS. The slices were blocked with 5% normal goat serum, followed by overnight incubation with streptavidin (1:500, Invitrogen) at 4°C. Slices were then washed 3× in 0.1 м PBS and incubated in Alexa 488 goat anti-mouse secondary Ab (1:500, Invitrogen) for 2−4 h at room temperature. After washes in 0.1 м PBS, slices were mounted on slides and embedded in a mounting medium (Mowiol). Maximum intensity z-stack images were taken using a confocal microscope (Leica DMI 6000) with a 20× oil immersion objective. For the histological image shown in the *Results*, eight maximum projection images of confocal stacks acquired at 20× magnification were stitched using the algorithm of Preibisch et al. (2009), available as a plugin in ImageJ (1.53c). In a subset of experiments, biocytin-filled cells were visualized with 3,3'-diaminobenzidine tetrahydrochloride (0.015%) using a standard ABC kit (Vectorlabs).

Results

To quantify the propagation of SPW-Rs in CA3 *in vitro*, we recorded extracellular correlates using MEAs and intracellular correlates using whole-cell patch-clamp electrodes.

MEA LFP recordings

In the first set of experiments, we performed MEA recordings in the CA3 area of hippocampal slices of mice (25 slices from eight animals, example in Fig. 1*A*). Across slices, SPW-Rs occurred spontaneously at a rate of 0.95 ± 0.45 s^{-1} (mean ± SD) with an amplitude of 0.046 ± 0.036 mV, and a duration of 31.3 ± 2.5 ms. Events recorded from or close to the *str. pyr.* were regularly overlaid by high-frequency oscillations in the ripple-frequency band (202.8 ± 5.7 Hz; see examples in Fig. 1*Ba*). These basic SPW-R properties were comparable across recording channels and SPW-R events.

To investigate the propagation of SPW-Rs, we focused on the low-frequency (5−40 Hz) SPW component and disregarded the finer structure of ripple oscillations (Fig. 1*Bb*). Across the MEA, the amplitude and polarity of the SPW depended on the position of each recording channel (Fig. 1*B*). Recording sites close to the cell body layer *str. pyr.* displayed positive SPW polarity, and these sites were selected as COIs; moreover, COIs were assigned a one-dimensional spatial coordinate (0−100%) that denotes their approximate position along the axis of the *str. pyr.* Here, 0% and 100% correspond to the starting and ending points of the pyramidal cell layer spanning from CA3c to CA3a (Fig. 1*Ac–d*; see also *Materials and methods*).

For each slice, the COI with the maximal average SPW amplitude was defined as the reference channel; for each SPW event and each COI, the relative arrival time of the SPW was determined by cross-correlating the LFP signal with the signal recorded at the reference channel and finding the time shift corresponding to maximal correlation (see *Materials and methods*). Cross-correlation was a reasonable way to determine delays because the waveforms at the COIs were similar (see the normalized waveforms in Fig. 1*Ca*). Linear regression over the relative arrival times at all COIs yields an estimate of the direction and speed of the propagation of a single SPW (example event in Fig. 1*Cb*). The histogram of single-event slopes of all SPWs in one slice is shown in Fig. 1*Da*. The histogram has a unimodal distribution with a significantly *positive* average slope (0.135 [0.13, 0.14] ms/%, mean and 99% bootstrap CI, black triangle and grey area in Fig. 1*Da*). Thus, in this slice, almost all SPWs propagate in the direction from CA3c toward CA3a.

Because the histogram of single-event slopes is unimodal without outliers, its mean slope represents the distribution well. We thus limited the statistical evaluation of the linear regression to the mean single-event slope (Fig. 1*Da*, triangle), which is mathematically equivalent to the result of a *single* linear regression across the *mean* SPW latencies (Fig. 1*Db*, black dots and continuous line). For the regression in Fig. 1*Db*, a standard statistical analysis assuming independent and identically normally distributed residuals yields a 99% CI for the slope of [0.09, 0.18] ms/%. However, since the variance of the SPW arrival latencies in our data appears to vary with recording location (variable spread of coloured dots in Fig. 1*Db*), we used a non-parametric permutation test to evaluate the statistical significance of the regression slope ($p = 1.5 \times 10^{-6}$; see also Table 1).

Note that we have quantified SPW propagation in milliseconds per percent of the CA3c-to-CA3a axis [ms/%] for better comparison across slices with CA3 of various sizes. In the example slice ID: 17 in Fig. 1, the length of CA3 *str. pyr.* was 1.87 mm, which means that SPWs propagated with an average slope of 7.2 s/m. The positive

Table 1. SPW propagation statistics for MEA recordings

Slice ID	# events	Slope [ms/%]	Confidence interval [ms/%]	*P*-value	Significance
12	880	0.150	[0.147, 0.154]	$9.9 \cdot 10^{-5}$	**
17	1127	0.135	[0.130, 0.141]	$1.5 \cdot 10^{-6}$	**
13	1086	0.130	[0.124, 0.137]	$0.0 \cdot 10^{0}$	**
14	125	0.126	[0.111, 0.142]	$1.8 \cdot 10^{-3}$	**
22	345	0.113	[0.102, 0.123]	$9.3 \cdot 10^{-4}$	**
11	178	0.091	[0.076, 0.106]	$8.3 \cdot 10^{-3}$	**
7	747	0.085	[0.081, 0.090]	$3.1 \cdot 10^{-8}$	**
3	273	0.083	[0.077, 0.090]	$2.5 \cdot 10^{-6}$	**
1	783	0.075	[0.073, 0.078]	$2.2 \cdot 10^{-4}$	**
19	352	0.073	[0.067, 0.079]	$1.3 \cdot 10^{-7}$	**
2	574	0.070	[0.067, 0.072]	$7.1 \cdot 10^{-5}$	**
9	615	0.067	[0.064, 0.071]	$1.2 \cdot 10^{-4}$	**
6	380	0.058	[0.055, 0.061]	$4.4 \cdot 10^{-5}$	**
8	143	0.055	[0.033, 0.072]	$2.1 \cdot 10^{-2}$	n.s.
25	508	0.050	[0.042, 0.057]	$9.8 \cdot 10^{-6}$	**
18	902	0.046	[0.041, 0.050]	$1.5 \cdot 10^{-3}$	**
4	337	0.044	[0.037, 0.052]	$4.1 \cdot 10^{-6}$	**
23	651	0.032	[0.026, 0.038]	$1.9 \cdot 10^{-3}$	**
21	1095	0.020	[0.014, 0.027]	$1.4 \cdot 10^{-1}$	n.s.
10	770	0.011	[0.010, 0.012]	$1.8 \cdot 10^{-1}$	n.s.
15	1224	0.002	[−0.000, 0.003]	$7.7 \cdot 10^{-1}$	n.s.
16	1178	−0.001	[−0.003, 0.001]	$9.2 \cdot 10^{-1}$	n.s.
24	499	−0.011	[−0.015, −0.006]	$4.6 \cdot 10^{-1}$	n.s.
5	171	−0.012	[−0.025, 0.001]	$3.2 \cdot 10^{-3}$	**
20	735	−0.020	[−0.023, −0.016]	$1.2 \cdot 10^{-2}$	n.s.

Note: Summary for 25 slices, sorted (from top to bottom) by mean regression slope, as in Fig. 2. Columns from left to right: Identification number of a slice (slice ID), number of SPW events analysed in a slice (# events), mean linear regression slope (Slope [ms/%]), 99% bootstrap CI for the mean of the single-event slopes, *p*-value for the linear regression over mean latencies (permutation test, see *Materials and methods*), significance rating with ** indicating $p < 0.01$ and n.s. denoting 'not significant'.

sign of the propagation slope indicates that SPWs tended to propagate in the direction from CA3c toward CA3a. A simple inverse of this average slope leads to an average propagation speed of 0.14 m/s, which is a reasonable estimate in slice ID: 17 because most SPW events propagate in the same direction. We would like to note, however, that the inverse of the average slope is, in general, not a good measure for the average propagation speed; this measure is problematic in slices in which the propagation is not significant, or can occur in both directions, and there are such examples in our population of 25 slices; for example, slices ID: 24 and 25.

A clear direction of propagation of SPWs (from CA3c toward CA3a) was found in a large fraction of the population of 25 slices (Fig. 2): on the left, the distributions of single-event propagation slopes are shown; in the middle, the average latencies of SPW arrivals at COIs with the corresponding regression lines are depicted (same layout as example in Fig. 1*D*).

We found that the distribution of regression slopes across events is largely unimodal in most slices (weak bimodality only in slice ID: 25 with peaks at about 0.10 and −0.05 ms/%) and that there are no outliers, which suggests that SPWs propagate consistently in a preferred direction in every slice and that the average slope characterizes this behaviour well (Fig. 2, left; note the small 99% bootstrap CIs of the mean (grey areas)).

Overall, we find that in 18 out of 25 slices, the regression slope is significantly different from 0 ($p < 0.01$ in Table 1, permutation test), that is, there *is* propagation of SPWs. The significant propagation of SPWs in these 18 slices occurs mostly in the direction from CA3c toward CA3a (17/18 slices, Fig. 2, topmost panels). Only one slice (ID: 5) displays significant propagation in the opposite direction, that is, from CA3a toward CA3c. However, the 99% bootstrap CI of slice ID: 5 is wide and includes zero slope, reflecting a large variability of propagation direction in single events (Fig. 2, left). Note that the propagation in slice ID: 20 (bottom of Fig. 2) is not significant ($p > 0.01$ in Table 1, permutation test).

Pooling together the mean slopes of all slices, we find a grand average slope of 0.059 [0.035, 0.084]
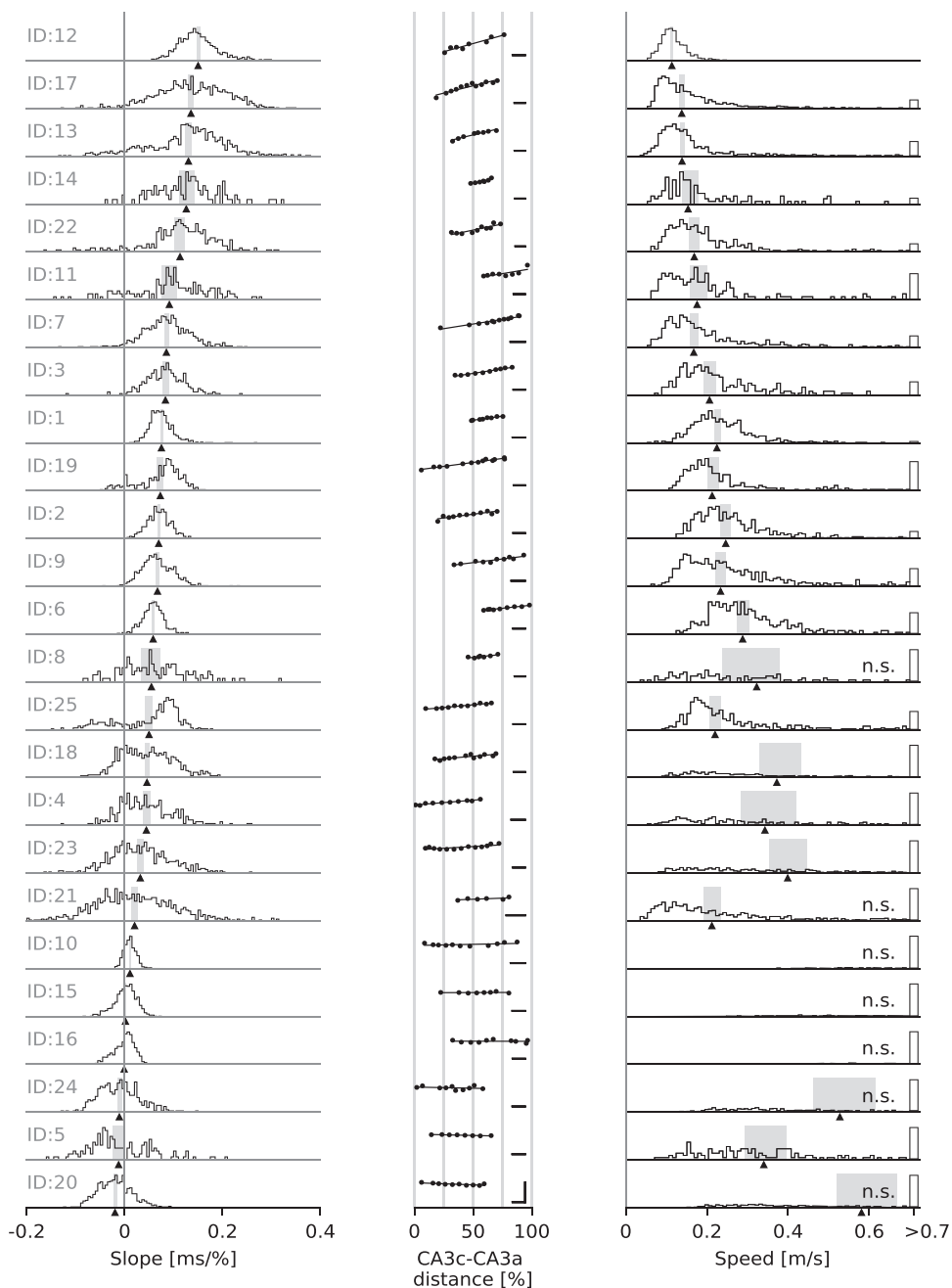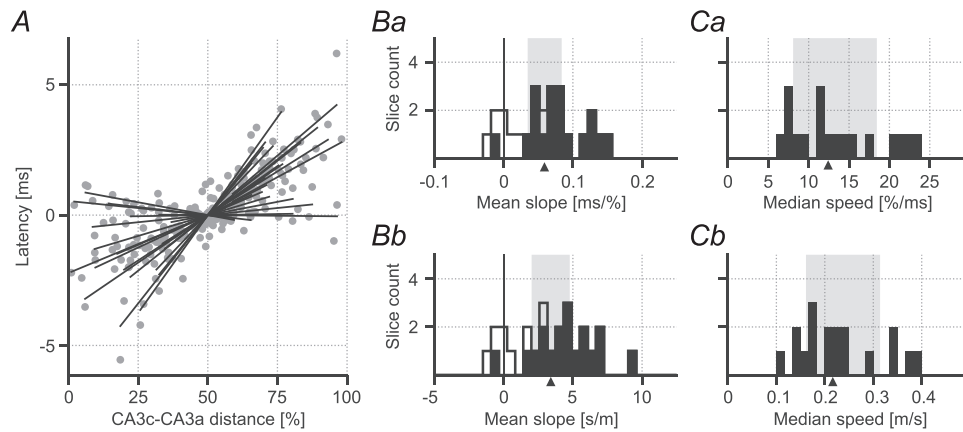
Figure 2. Propagation of SPWs across CA3 derived from MEA recordings
Linear regression over SPW arrival latencies for 25 slices (top to bottom, sorted by mean regression slope). *Left*, distribution of regression slopes for individual SPW events. Triangle: mean regression slope; grey area: 99% bootstrap CI (cf. Table 1). *Middle*, linear regression (line) over average SPW arrival latencies (circular markers) at channels of interest. Vertical scale bar (only for slice ID: 20 at bottom) and horizontal scale bars mark 10 ms and 200 μm, respectively. *Right*, distribution of single-event propagation speeds (in m/s). High outlier speeds (>0.7 m/s) correspond to small propagation slopes and are summarized in the last bin. Triangles mark median speeds (beyond axis limit for slices ID: 10, 15, 16), shaded areas indicate 99% bootstrap CIs. Slices with a mean propagation slope *not* significantly different from zero are marked as 'n.s.'.

ms/% (mean and 99% bootstrap CI, Fig. 3*A* and *Ba*). The length estimates for the curved *str. pyr.* structure were approximately unimodally distributed across slices (median: 1.66 mm, [Q1, Q3]: [1.60, 1.79] mm, range: [1.14, 2.02] mm). Taking into account these different sizes of the CA3 areas, we find a grand average slope of 3.4 [2.0, 4.8] s/m (mean and 99% bootstrap CI, Fig. 3*Bb*).

Figure 3. Summary of propagation of SPWs in CA3 derived from MEA recordings
Average SPW propagation slopes from all slices indicate mostly propagation of SPWs in the direction from CA3c toward CA3a. *A*, combined linear regression results of all slices. Average arrival latencies and regression lines (Fig. 2, middle) were shifted to a common reference point of 0 ms latency in the centre (50%) of the CA3c–CA3a axis. *B*, histogram of mean propagation slopes in ms/% (triangles in Fig. 2, left) (*Ba*) or in s/m (*Bb*). Empty bars show data from slices with a mean slope not significantly different from zero (∼ no propagation, marked as 'n.s.' in Fig. 2 and Table 1). Triangle and grey area mark overall mean and 99% bootstrap CI, respectively. *C*, histogram of median propagation speeds in %/ms (*Ca*), or in m/s (triangles in Fig. 2, right) (*Cb*). Speed data are shown only for slices with a mean slope significantly different from zero (black bars in *B*). Triangles and grey boxes mark corresponding median and 99% bootstrap CIs, respectively.

Next, we estimated the propagation *speed* (in m/s) for all events (Fig. 2, right). These speeds were derived as the inverse of the absolute slopes (Fig. 2, left) to account for the speed of propagation independent of its direction. Furthermore, we took into account the sizes of the respective slices (spatial scale bars in Fig. 2, middle). Note that SPW events with propagation slope close to zero (∼ no propagation) contribute large outlier values to the speed distribution (rightmost bins summarizing speeds >0.7 m/s in Fig. 2, right). Thus, in slices with many such events, the median speed is larger than the mode of the speed distribution. Pooling together the median speeds from slices with significant propagation (non-zero mean slopes, see Table 1), we found a grand average propagation speed of 0.22 [0.16, 0.31] m/s (median and 99% bootstrap CI, Fig. 3*Cb*). For normalized sizes of the slices, the grand average propagation speed (in %/ms) was 12.4 [8.1, 18.4] %/ms (median and 99% bootstrap CIs, Fig. 3*Ca*).

Combined LFP and whole-cell experiments

To understand synaptic properties of neuronal network patterns such as SPWs beyond the analysis of their LFP signatures, the study of the corresponding intracellular activity is inevitable. Focusing on synaptic activity in CA3 pyramidal neurons, previous work has investigated the intracellular correlates of SPWs using whole-cell patch-clamp recordings (Hájos et al., 2013; Kajikawa et al., 2022; Swaminathan et al., 2018). In particular, whole-cell recordings in the voltage-clamp configuration can be used

to separate the excitatory (mostly sodium-driven) from the inhibitory (mostly chloride-driven) components of the cPSCs underlying SPWs with high temporal accuracy (Donoso et al., 2018; Maier et al., 2011).

Therefore, to also investigate the propagation of SPWs in CA3 at the level of associated synaptic activity, we performed simultaneous whole-cell recordings of two or three pyramidal cells in different CA3 subfields (Fig. 4*A*). These experiments were performed in electrophysiological experimental setups that allowed visual identification of the cells of interest and were equipped with devices for recording up to three cells (see *Materials and methods*). A total of 32 slices from 21 mice were recorded, including 30 slices with two-cell recordings and two slices with three-cell recordings. In all experiments, an additional electrode was used to record the LFP to capture spontaneously occurring SPW-Rs (Fig. 4*B* and *C*). Across slices, SPW-Rs occurred spontaneously at a rate of 0.74 ± 0.40 s^{-1} (mean $\pm$ SD), with an amplitude of 0.22 ± 0.14 mV, a duration of 34.4 ± 7.6 ms, and these events regularly displayed oscillations in the $120-250$ Hz ripple-frequency band (195.3 ± 6.8 Hz; see examples in Fig. 4*C*), largely comparable to the recordings in our MEA experiments.

Consistent with earlier reports (Ellender et al., 2010; Hájos et al., 2013; Swaminathan et al., 2018), voltage-clamp recordings near the inhibitory reversal potential (≈ -60 mV) showed compound inward (excitatory) postsynaptic currents (cEPSCs) in temporal association with extracellular SPWs (Fig. 4*Ba*). Likewise, recordings near the excitatory reversal potential
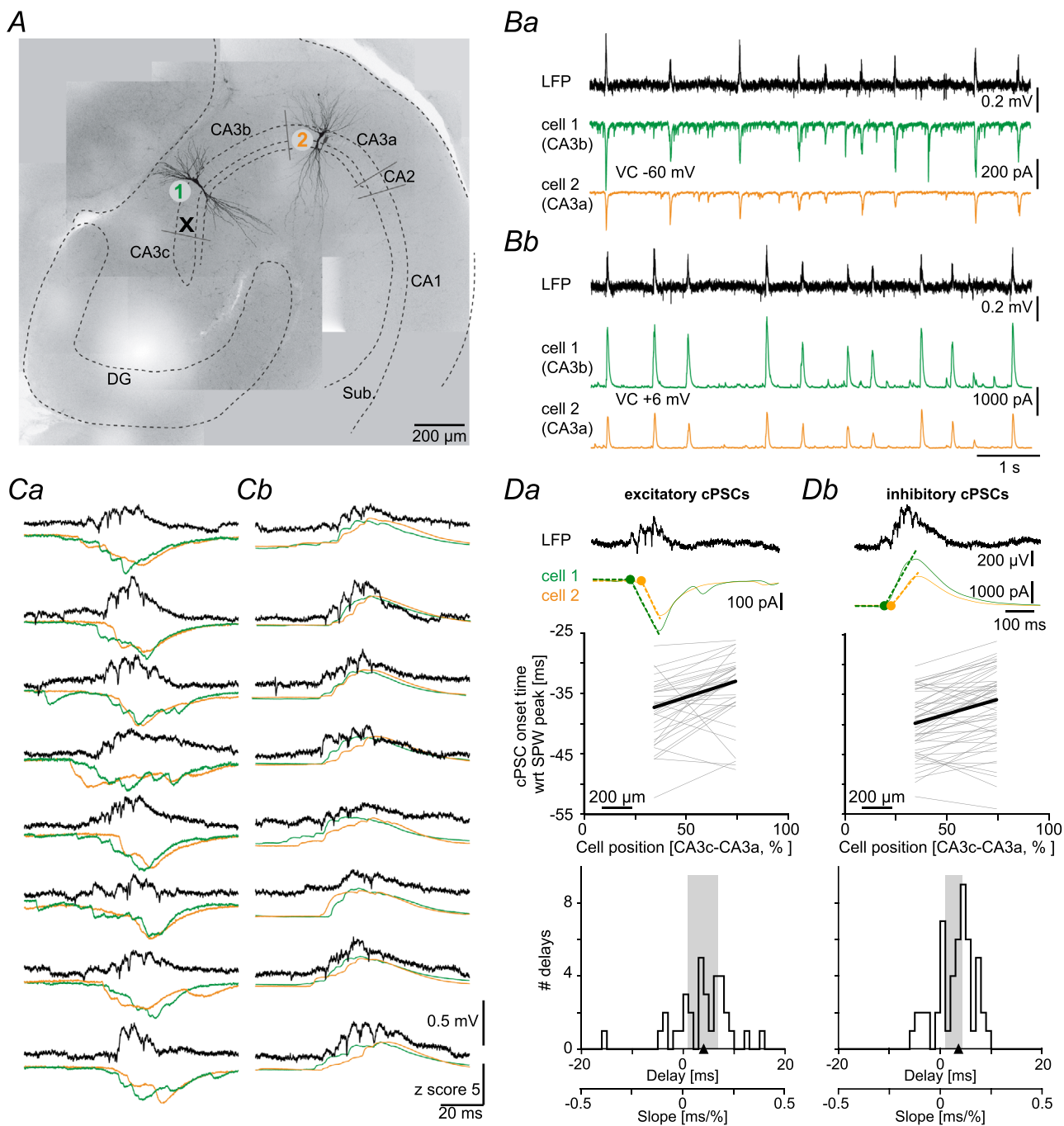
Figure 4. Spread of SPW-associated postsynaptic currents in pyramidal neurons within CA3

A, illustration of an example experiment (slice ID: 31) with recordings from pyramidal cells in CA3b (cell 1) and CA3a (cell 2). The bold '×' indicates the approximate position of the field potential recording electrode. Dashed lines delineate the approximate structures of the hippocampus, and grey solid lines indicate the approximate boundaries between CA subfields. Abbreviations: DG, dentate gyrus; CA3c–a, CA3 area with subfields *c*, *b* and *a*; Sub., subiculum. *B*, dual whole-cell and field potential recordings taken from the experiment illustrated in (*A*). Panel (*Ba*) shows an episode where both cells were voltage clamped (VC) at −60 mV. Panel (*Bb*) displays an episode where both cells were voltage clamped at +6 mV. *C*, example individual field potential SPW-Rs (black) and their associated compound excitatory (*Ca*) and inhibitory (*Cb*) postsynaptic currents (coloured) simultaneously recorded in cell 1 and cell 2 corresponding to the periods of recordings shown in (*Ba*) and (*Bb*). The postsynaptic current traces were z-scored to highlight the temporal dynamics of signals from both cells, rather than their differences in amplitude. *D, top*, example LFP SPW-Rs (black) and corresponding low-pass filtered traces (coloured) for cEPSCs (*Da*) and cIPSCs (*Db*) with fits (dashed lines) used to determine the respective onset times (green and orange dots). *Middle* and *bottom*, line plots of cPSC onset times and histograms of onset time delays/slopes for cEPSCs (*Da*) and

cIPSCs (*Db*). Data summarize the experiment displayed in panels (*A–C*). In the middle panels of (*D*), the grey lines represent individual SPW events, and the bold black lines are averages; in the bottom panels, the triangle and grey area mark corresponding median and 99% bootstrap CI, respectively.

($\approx$+6 mV) showed compound outward (inhibitory) postsynaptic currents (cIPSCs) during SPWs (Fig. 4*Bb*).

For every SPW-R event detected in the LFP, the timing of the SPW-associated cEPSCs or cIPSCs was estimated (Fig. 4*C*). This estimate was not straightforward because the shapes of cEPSCs or cIPSCs across cells were highly variable (*e.g.* Fig. 4*C*). This variability was much larger than the variability of the shapes of the LFP signals across different MEA channels (see, *e.g.* Fig. 1*Da*). Therefore, for the analysis of whole-cell recordings, we could not use simple cross-correlation to estimate the SPW propagation delay. Instead, we first estimated the *onset* times of cEPSCs or cIPSCs with respect to the peak of the SPW in the LFP (see *Materials and methods*, Fig. 4*D*, top). The propagation direction was then inferred by either simple subtraction of the onset times of two cells (examples in Fig. 4*D*) or, in the case of three simultaneously recorded cells, by linear regression. In the example traces shown in Fig. 4*Ca* and *Da*, the onsets of cEPSCs of cell 1 (green) were mostly before the ones of cEPSCs of cell 2 (orange) with a delay of 4.59 [2.53, 7.05] ms (median and 99% bootstrap CI); a similar order of onsets was observed for cIPSCs with a delay of 3.87 [3.14, 5.22] ms (median and 99% bootstrap CI; Fig. 4*Cb* and *Db*).

To determine the direction of propagation, each cell was assigned a one-dimensional spatial coordinate (0–100%) indicating the approximate position of its soma along the CA3c-to-CA3a axis of the *str. pyr.* (*see Materials and methods*, examples in Fig. 4*A*). Dividing by the distance between the cells along the curved *str. pyr.* axis, we converted the delay between the SPW-associated cEPSCs or cIPSCs to an approximate SPW propagation *slope* [ms/%]. In the example slice shown in Fig. 4, the distributions of propagation slopes for cEPSCs and cIPSCs (Fig. 4*D*, bottom) both showed a clear trend toward positive values (median slope and 99% bootstrap CI: 0.11 [0.06, 0.18] ms/% for cEPSCs; 0.10 [0.08, 0.13] ms/% for cIPSCs), suggesting a propagation of SPW-associated synaptic activity, and hence SPWs, in the direction from CA3c toward CA3a. The length of CA3 *str. pyr.* in this slice was 1.35 mm, so that the median slopes can be converted to 8.52 s/m for cEPSCs and 7.19 s/m for cIPSCs.

The results obtained for the propagation of SPWs in the example slice (Fig. 4) are similar in a large fraction of the population of 32 slices (Fig. 5): in the middle panel, median arrival latencies of cEPSCs (black dots) and cIPSCs (blue dots) and slopes (lines) are shown (similar to the example in Fig. 4*D*, middle). To test whether the propagation of SPWs as inferred from averages over many events recorded in a slice is representative, we also show histograms of slopes associated with individual SPWs (Fig. 5, left; similar to the example in Fig. 4*D*, bottom). Histograms for cEPSCs (black) and cIPSCs (blue) are overlaid. Almost all slices exhibit roughly unimodal slope distributions (exception: slice ID: 26, seventh from bottom). The median slopes obtained from the histograms (Fig. 5, left, triangles) correspond very well to the slopes obtained from median arrival latencies (Fig. 5, middle) with Pearson correlation coefficients >0.99 for both excitation and inhibition. Again, we estimated propagation *speed* (in m/s) for all events as the inverse of the absolute slopes, taking into account the size of the respective slices (Fig. 5, right). The lengths of CA3 *str. pyr.* were distributed approximately unimodally across slices (median: 1.37 mm, [Q1, Q3]: [1.29, 1.56] mm, range: [1.10, 1.87] mm, see also spatial scale bars in Fig. 5, middle).

To assess the direction of propagation, we return to slopes (without rectification). There is a preferred direction of propagation of SPWs in 22/29 slices for cEPSC recordings and in 28/31 slices for cIPSC recordings (median slope significantly different from 0, $p < 0.01$, two-sided one-sample Wilcoxon signed-rank test; see Table 2). Pooling together the median slopes of all slices, we find positive grand average slopes of 0.035 [−0.047, 0.085] ms/% for excitation (Fig. 6*Aa*) and 0.109 [0.048, 0.159] ms/% for inhibition (Fig. 6*Ab*), suggesting a predominant direction of SPW propagation in the direction from CA3c toward CA3a. Taking into account the different sizes of the CA3 areas in different slices and measuring distances in millimetres yields grand average slopes of 3.06 [−3.20, 6.58] s/m (median and 99% CI) for excitation (Fig. 6*Ba*) and 7.19 [3.59, 11.22] s/m (median and 99% CI) for inhibition (Fig. 6*Bb*).

Pooling together the median *speeds* from slices with significant propagation (non-zero median slopes, see Table 2), we find a grand average propagation speed of 0.14 [0.10, 0.20] m/s for excitation (Fig. 6*Ea*) and 0.09 [0.08, 0.13] m/s for inhibition (Fig. 6*Eb*). For normalized sizes of slices, we find grand average median propagation speeds of 10.74 [7.01, 14.04] %/ms for excitation (Fig. 6*Da*) and 6.85 [5.68, 9.69] %/ms for inhibition Fig. 6*Db*).

In 28 out of 32 slices, both excitatory and inhibitory currents were measured. In many slices the corresponding histograms of slopes showed a large overlap (Fig. 5, left), so we asked whether the results of our SPW propagation analysis were generally correlated between excitatory and inhibitory measurements. For this analysis, we considered *mean* propagation slopes, which were highly correlated to the medians ($r = 0.970$ for cEPSCs, $r = 0.974$ for
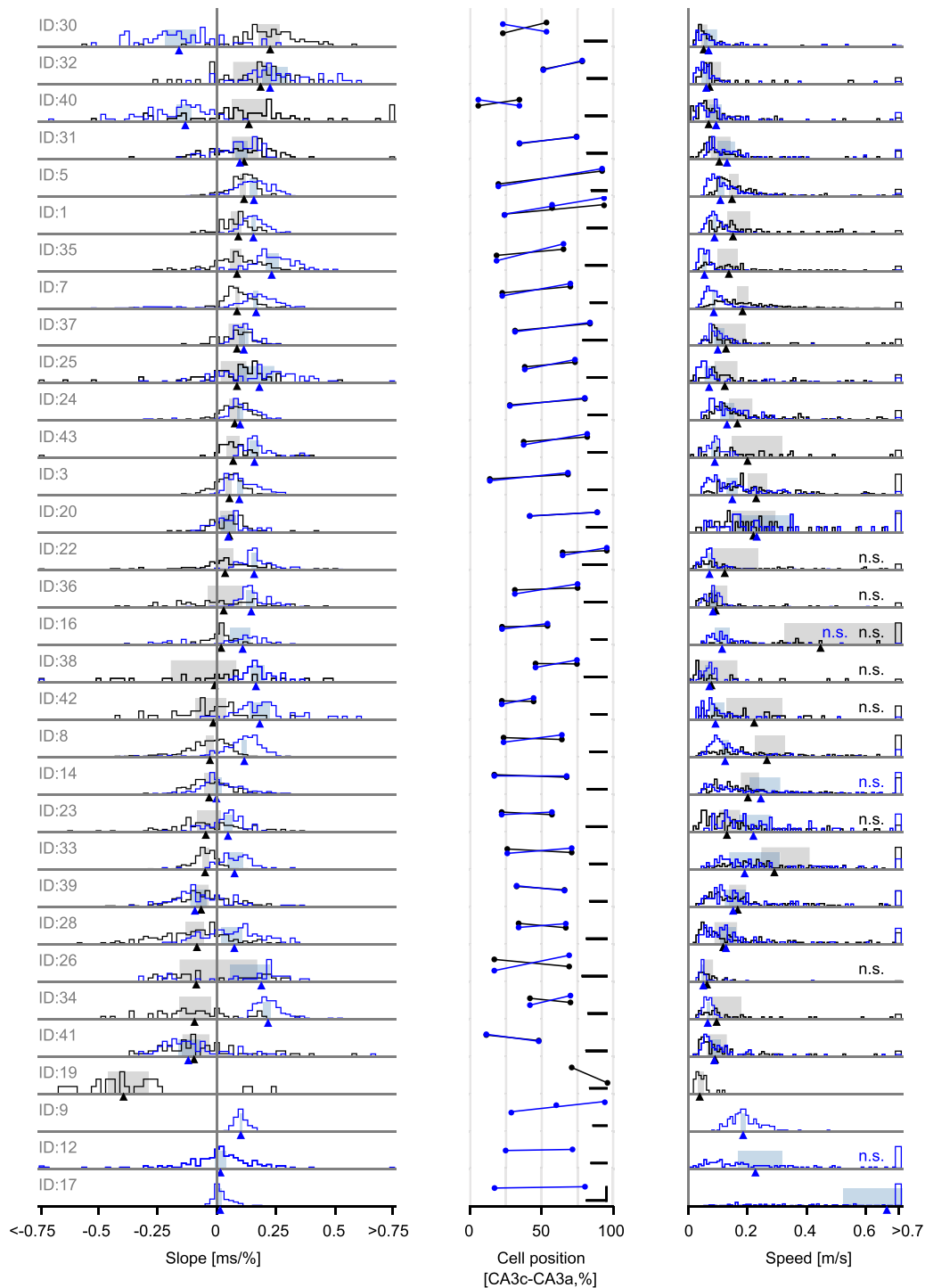
Figure 5. Propagation of SPW-associated excitatory and inhibitory postsynaptic currents across CA3
Left, distribution of single-event propagation slopes derived from excitatory (black) or inhibitory (blue) cPSCs. Triangles mark median slopes. Light grey and blue shaded boxes indicate 99% bootstrap CI (cf. Table 2). Results are shown for all 32 slices, sorted by the median propagation slope for excitatory cPSC recordings (top to bottom). Outlier slopes (absolute value >0.75 ms/%) are summarized in first and last bins. There were only 14 outliers overall (slice ID: 12, 22, 25, 31, 38, 40, 43). *Middle*, median SPW arrival latencies derived from excitatory (black) or inhibitory (blue) cPSCs. Line indicates propagation slope (linear regression in case of three cells: IDs 1, 9). Vertical scale bar (only for slice ID:17 at bottom) and horizontal scale bars mark 10 ms and 200 μm, respectively. *Right*, distribution of single-event propagation speeds derived from excitatory (black) or inhibitory (blue) cPSCs as the

inverse of the absolute value of the slope (in m/s). Triangles mark median speeds. Light grey and light blue shaded areas indicate 99% bootstrap CI. High outlier speeds (absolute value >0.7 m/s) correspond to small propagation slopes and are summarized in the rightmost bins.

Table 2. SPW propagation statistics for whole-cell recordings

Slice ID	Compound excitatory postsynaptic current (cEPSC) recordings					Compound inhibitory postsynaptic current (cIPSC) recordings				
	# events	Slope [ms/%]	Confidence interval [ms/%]	*P*-value	Signi-ficance	# events	Slope [ms/%]	Confidence interval [ms/%]	*P*-value	Signi-ficance
30	88	0.225	[0.177, 0.264]	$1.1 \cdot 10^{-13}$	**	56	−0.160	[−0.222, −0.091]	$6.8 \cdot 10^{-7}$	**
32	40	0.184	[0.058, 0.224]	$2.4 \cdot 10^{-5}$	**	51	0.224	[0.182, 0.292]	$1.1 \cdot 10^{-9}$	**
40	75	0.135	[0.050, 0.198]	$3.3 \cdot 10^{-5}$	**	88	−0.133	[−0.171, −0.109]	$4.5 \cdot 10^{-15}$	**
31	78	0.115	[0.057, 0.169]	$2.1 \cdot 10^{-8}$	**	93	0.097	[0.073, 0.128]	$6.3 \cdot 10^{-12}$	**
5	167	0.115	[0.098, 0.124]	$2.1 \cdot 10^{-27}$	**	242	0.156	[0.139, 0.171]	$7.0 \cdot 10^{-41}$	**
1	67	0.090	[0.058, 0.102]	$1.1 \cdot 10^{-10}$	**	349	0.154	[0.145, 0.163]	$5.9 \cdot 10^{-59}$	**
35	109	0.085	[0.056, 0.102]	$2.9 \cdot 10^{-10}$	**	96	0.231	[0.205, 0.259]	$2.0 \cdot 10^{-17}$	**
7	391	0.085	[0.078, 0.094]	$4.9 \cdot 10^{-57}$	**	544	0.166	[0.153, 0.174]	$2.4 \cdot 10^{-35}$	**
37	50	0.085	[0.049, 0.118]	$2.5 \cdot 10^{-7}$	**	61	0.114	[0.092, 0.129]	$1.1 \cdot 10^{-11}$	**
25	62	0.085	[0.015, 0.125]	$2.0 \cdot 10^{-3}$	**	84	0.179	[0.087, 0.241]	$2.5 \cdot 10^{-10}$	**
24	147	0.076	[0.051, 0.095]	$2.4 \cdot 10^{-15}$	**	151	0.098	[0.083, 0.112]	$1.1 \cdot 10^{-14}$	**
43	39	0.069	[0.041, 0.095]	$2.6 \cdot 10^{-6}$	**	43	0.159	[0.137, 0.179]	$1.1 \cdot 10^{-8}$	**
3	335	0.053	[0.038, 0.063]	$3.4 \cdot 10^{-27}$	**	303	0.095	[0.085, 0.108]	$2.9 \cdot 10^{-49}$	**
20	56	0.052	[0.004, 0.079]	$1.3 \cdot 10^{-4}$	**	50	0.048	[0.016, 0.079]	$7.1 \cdot 10^{-5}$	**
22	84	0.035	[0.003, 0.071]	$1.2 \cdot 10^{-2}$	n.s.	111	0.157	[0.146, 0.168]	$1.1 \cdot 10^{-19}$	**
36	66	0.029	[−0.038, 0.103]	$2.0 \cdot 10^{-1}$	n.s.	95	0.145	[0.123, 0.156]	$6.5 \cdot 10^{-17}$	**
16	52	0.018	[−0.001, 0.031]	$4.6 \cdot 10^{-2}$	n.s.	58	0.109	[0.049, 0.138]	$6.8 \cdot 10^{-2}$	n.s.
38	28	−0.009	[−0.195, 0.082]	$6.5 \cdot 10^{-1}$	n.s.	36	0.165	[0.141, 0.197]	$3.1 \cdot 10^{-6}$	**
42	42	−0.016	[−0.090, 0.040]	$1.7 \cdot 10^{-1}$	n.s.	52	0.181	[0.134, 0.222]	$7.0 \cdot 10^{-10}$	**
8	349	−0.029	[−0.046, −0.017]	$2.4 \cdot 10^{-12}$	**	401	0.116	[0.104, 0.126]	$4.7 \cdot 10^{-39}$	**
14	309	−0.033	[−0.053, −0.017]	$4.1 \cdot 10^{-7}$	**	341	−0.002	[−0.011, 0.021]	$1.6 \cdot 10^{-2}$	n.s.
23	102	−0.047	[−0.086, 0.015]	$1.6 \cdot 10^{-2}$	n.s.	86	0.047	[0.026, 0.064]	$2.1 \cdot 10^{-5}$	**
33	148	−0.050	[−0.062, −0.034]	$5.9 \cdot 10^{-19}$	**	62	0.075	[0.041, 0.108]	$1.1 \cdot 10^{-8}$	**
39	168	−0.067	[−0.089, −0.036]	$2.2 \cdot 10^{-8}$	**	100	−0.093	[−0.113, −0.043]	$4.9 \cdot 10^{-7}$	**
28	139	−0.084	[−0.132, −0.055]	$1.9 \cdot 10^{-12}$	**	107	0.074	[0.016, 0.105]	$1.2 \cdot 10^{-6}$	**
26	29	−0.087	[−0.173, 0.164]	$9.1 \cdot 10^{-1}$	n.s.	39	0.188	[0.055, 0.221]	$9.8 \cdot 10^{-3}$	**
34	49	−0.094	[−0.165, −0.033]	$5.7 \cdot 10^{-4}$	**	138	0.216	[0.196, 0.228]	$2.2 \cdot 10^{-24}$	**
41	72	−0.097	[−0.148, −0.037]	$1.6 \cdot 10^{-3}$	**	79	−0.121	[−0.169, −0.076]	$4.3 \cdot 10^{-6}$	**
19	27	−0.394	[−0.495, −0.292]	$1.2 \cdot 10^{-5}$	**					
9						182	0.101	[0.096, 0.105]	$1.3 \cdot 10^{-31}$	**
12						145	0.015	[−0.010, 0.035]	$2.7 \cdot 10^{-1}$	n.s.
17						184	0.014	[0.008, 0.021]	$1.5 \cdot 10^{-14}$	**

Note: Summary for 32 slices sorted (from top to bottom) by the median propagation slope for cEPSC recordings, as in Fig. 5. Left: cEPSC recordings, right: cIPSC recordings. Columns from left to right: Identification number of a slice (slice ID), number of SPW events included in the analysis (# events), median propagation slope (Slope [ms/%]), 99% bootstrap CI, *p*-value (two-sided one-sample Wilcoxon signed-rank test) and corresponding significance rating for all slices ($\alpha = 0.01$, n.s. for non-significant). We found that for a significance level $\alpha = 0.01$ the CIs were consistent with the results of the two-sided one-sample Wilcoxon signed rank test, in the sense that the CI of the median did not contain zero for slices with $p < 0.01$. Significance asterisks (**) hence indicate slices with $p < 0.01$ and a CI of the median slope that does not include zero.

cIPSCs). The mean slopes (black markers in Fig. 6*C*), together with the associated standard errors of the mean (SEM, error bars in Fig. 6*C*), are amenable to an advanced, *weighted* linear regression analysis that takes into account the variable uncertainties of the slope estimates across slices and excitatory/inhibitory recordings (Tellinghuisen, 2020). This weighted linear regression indicates a strong correlation between the mean propagation slopes for cEPSCs and cIPSCs (regression slope and 99% bootstrap CI: 1.13 [1.01, 1.27], black line in Fig. 6*C*). This result reflects the majority of slices that fall into quadrants 1 and 3; that is, for which cEPSCs and cIPSCs suggest the *same* direction and a similar speed of propagation, often with small uncertainty (quadrant 1: 15 slices, quadrant
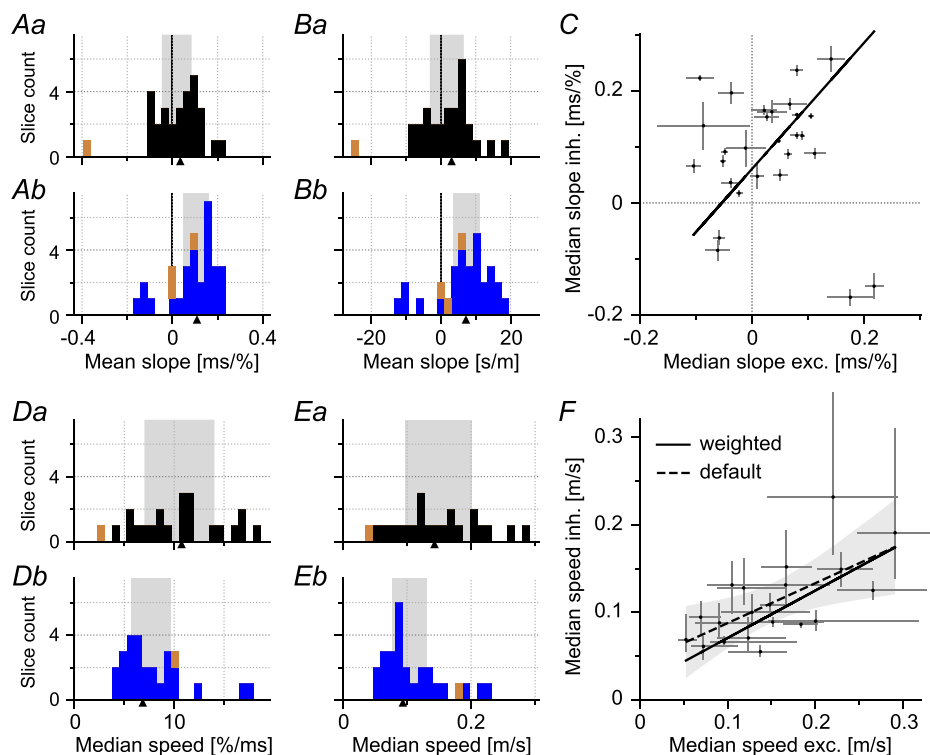
Figure 6. Summary of propagation of SPWs in CA3 using whole-cell recordings
Regression slopes (*A–C*) and speeds (*D–F*) derived from excitatory (black) and inhibitory (blue) cPSCs, respectively. Triangles and light grey areas indicate overall medians and 99% bootstrap CIs. *A*, median regression slopes in ms/% for excitation (*Aa*) and inhibition (*Ab*), as in Fig. 5, left. *B*, median regression slopes in s/m for excitation (*Ba*) and inhibition (*Bb*). *C*, mean propagation slope derived from cIPSCs plotted against mean slope from cEPSCs. Each marker represents one slice in which both measurements were made (cf. Fig. 5). Error bars mark SEM. Continuous line: linear regression weighted by SEM. *D*, median propagation speeds in %/ms for excitation (*Da*) and inhibition (*Db*). *E*, median propagation speeds in m/s for excitation (*Ea*) and inhibition (*Eb*), as in Fig. 5, right. Slices with median propagation slope not significantly different from 0 (marked 'n.s.' in Fig. 5, right) are excluded in (*D–F*). The outlier median speed of slice ID: 17 is not shown in *Db* and *Eb* but contributes to the overall median. *F*, median propagation speed from cIPSCs against those from cEPSCs. Markers represent slices in which both median slopes were significantly different from zero. Error bars mark CIs in Fig. 5, right. Both default (dashed line) and weighted linear regression (continuous line) indicate a strong correlation. Brown bars in (*A*) and (*B*) and (*D*) and (*E*) represent slices where either excitatory or inhibitory activity (but not both) was recorded (four slices at bottom of Fig. 5), that is, data which is not included in (*C*) and (*F*).

3: 2 slices). A simple, unweighted linear regression yields no significant correlation between the propagation slopes of cEPSCs and cIPSCs (regression slope and 99% CI: -0.16 [$-0.85, 0.53$], $r^2 = 0.02$). Propagation *speed*, on the other hand, is highly correlated across cIPSC and cEPSC measurements, both for default and weighted linear regression (default linear regression with $r^2 = 0.44$ and regression slope and 99% CI 0.46 [0.10, 0.81]; weighted linear regression with regression slope and 99% bootstrap CI 0.54 [0.4, 0.71]; Fig. 6*F*).

The age of the mice analysed in this study ranged from 3 to 9 weeks. It has been shown that the occurrence of SPW-R events and the ripple frequency are stable from the third week of age onwards (Buhl & Buzsáki, 2005; Buzsáki, 2015; Wong et al., 2005). In a subset of whole-cell experiments, we tested for possible correlations between SPW propagation speed/directionality, and age. Neither

parameter showed a clear correlation. More specifically, a linear regression of median SPW propagation slope *vs*. age resulted in $r = 0.10, p = 0.612$ for cEPSCs ($n = 28$ slices) and $r = -0.07, p = 0.721$ for cIPSCs ($n = 30$ slices); a linear regression of median SPW propagation speed *vs*. age resulted in $r = 0.39, p = 0.042$ for cEPSCs and $r = -0.09$, $p = 0.630$ for cIPSCs. We conclude that the age of the mice included in our study had no substantial effect on our results.

Discussion

Here we used an *in vitro* slice model to characterize the propagation of a self-organized population pattern – sharp wave/ripple activity – in the CA3 field of the hippocampus. We found (1) that sharp waves do not

occur simultaneously throughout CA3, but rather arise locally and propagate through the subfield. (2) The preferred direction of propagation varied across different slices, but was most common in the direction from CA3c toward CA3a. (3) The preferred direction of propagation was the same in MEA-LFP measurements and in intracellular recordings when SPW-associated excitatory or inhibitory cPSCs were compared in pyramidal cells at different sites in CA3. In addition, (4) the spread direction of excitatory and inhibitory synaptic activity was found to be correlated in most slices. Finally, (5) our comparison of propagation of LFP SPWs and SPW-associated synaptic activity suggests similar propagation velocities (MEA: 0.22 m/s; cEPSCs: 0.14 m/s and cIPSCs: 0.09 m/s).

In spite of technical differences between the two approaches used to record field potentials (*i.e.* MEA and glass-pipette recordings), the properties of SPW-Rs recorded in the LFP were largely comparable. An exception was the SPW amplitude, which was larger in the glass-pipette/whole-cell experiments than in the MEA recordings. This could be related to the fact that the glass-pipette field potential electrode *within* the slice recorded the signal from the surrounding three-dimensional tissue volume whereas the planar MEA recording electrodes recorded signals from the lower surface of the slice and thus from the outside of the tissue block, which inevitably results in smaller voltages. Moreover, all SPW properties determined in MEA recordings are reported as averages across recording COIs. This includes channels further away from the *str. pyr.* and thus leads to a more conservative estimate of the SPW amplitude. The incidence of SPWs was not statistically different between MEA and glass-pipette recordings ($p = 0.08$, two-sample *t*-test) even though there is better tissue oxygenation in perforated MEAs (Egert et al., 2005) compared with conventional slice recordings in submersion chambers, which is expected to affect incidence.

The grand average SPW propagation slopes derived from MEA and whole-cell recordings were similar. However, the distribution of SPW propagation slopes across individual events was broader for the whole-cell than for the MEA recordings. This is likely related to differences in spatial sample size and the signal that was used to infer the propagation slope: in the MEA recordings propagation slopes were inferred from SPW arrival latencies measured in the LFP at many different recording sites along the proximo-distal *str. pyr.* axis. The LFP signal likely reflects an average of the network activity surrounding each of the electrodes. Intracellular recordings, on the other hand, were only made for 2−3 cells simultaneously and may be less reflective of the local network state. The spatial sample size could be increased in future experiments using a multineuron patch-clamp approach (Peng et al., 2019).

It is worth mentioning that our analysis assumes approximately *linear* propagation in *one direction* along the curved *str. pyr.* axis, and within the horizontal plane in which slices were cut. There were three slices (ID: 10, 16, 24) in the MEA recording data set in which visual inspection of the SPW arrival latencies suggested the emergence of a SPW in a central portion of CA3b, followed by an outwards propagation toward both ends of CA3 (CA3a and CA3c). Such simultaneous outward propagation, as well as other nonlinear patterns, cannot be captured by our linear regression analysis. For the same reason, our estimates of propagation speed should be interpreted with caution. In most slices (22/25), however, the assumption of linearity appeared to be well justified. Furthermore, the estimated propagation speeds are broadly consistent with the speed of action potential propagation in CA3 pyramidal cell axons (∼0.16–0.5 m/s, Meeks & Mennerick, 2007; Miles et al., 1988; Soleng et al., 2003).

Although we found some variability in the propagation slopes, the observed preference for spread in the direction from CA3c toward CA3a suggests a non-random origin of SPWs within CA3. In agreement with our results, Bazelot et al. (2016) showed that SPWs can arise at multiple sites in CA3 *in vitro*, with a higher probability of emerging toward CA3c than toward CA3a (their Fig. 6*C*). Since our recordings were rarely performed in CA3c proper, but rather at the proximal end of CA3b, we cannot resolve here whether SPWs originated in CA3c or proximal CA3b.

Previous *in vivo* studies reached different conclusions regarding SPW origin and propagation: using spiking activity of multiple units in CA3 that are temporally related to ripples in CA1, Csicsvari et al. (2000) demonstrated that spike activity in the CA3a field preceded that in the CA3b and CA3c fields; moreover, Oliva et al. (2016) showed that deep pyramidal neurons in the CA2 field increase their activity preceding ripples in CA3 and CA1, especially during wake ripples. Two factors may account for these apparent differences from the present results: (1) The aforementioned studies were performed on the dorsal hippocampus *in vivo*, whereas our recordings and those of Bazelot et al. (2016) were obtained from *ex vivo* slices taken from the middle to ventral part of the hippocampus. While the coupling of ripples across the dorsoventral extent of the hippocampus has been demonstrated (De Filippo & Schmitz, 2023; Nitzan et al., 2022; Patel et al., 2013), the spread of SPW-R activity between subfields, specifically in the more ventral hippocampus, has not, to our knowledge, been studied. Therefore, the difference in propagation could reflect differences in network dynamics along the dorsoventral axis of the hippocampus. (2) The hippocampus is embedded in the broader brain architecture *in vivo*, leading to a strong bias of hippocampal network activity, including SPW-Rs, by external inputs under natural

conditions (Kajikawa et al., 2022; Ramirez-Villegas et al., 2015; Yamamoto & Tonegawa, 2017; Zutshi & Buzsáki, 2023). Notably, the slice model lacks these functional inputs. As a result, our findings, along with the corresponding observations made by Bazelot et al. (2016) may elucidate the intricacies of intrahippocampal, local circuit dynamics that underlie the initiation and propagation of SPW-Rs, whereas results obtained *in vivo* may in addition emphasize the significance of extrahippocampal projections and their modulation of hippocampal network dynamics in orchestrating these intricate processes.

Finally, experiments and computational models have suggested that there is an interaction of excitatory and inhibitory neurons underlying the generation of SPWs in CA3 (Ellender et al., 2010; Evangelista et al., 2020; Schlingloff et al., 2014). Thus, the directional preference of SPW propagation observed in the present study is likely mediated by differences in the circuit architecture along the different subsections of CA3. Models for travelling waves typically rely on distance-dependent axonal delays (Ko & Ermentrout, 2007; Muller et al., 2018) and also distance-dependent connectivity (Miles et al., 1988; Sammons et al., 2024; Taxidis et al., 2012). The simulations by Taxidis et al. (2012) on propagation of SPW-like activity in CA3 along the longitudinal axis (with an assumed conduction velocity of 0.5 m/s of CA3 pyramidal cell axons) predicted a propagation velocity of about 0.15 m/s in a purely excitatory network; similarly, in the simulations by Traub et al. (1989) an axon conduction velocity of recurrent excitatory collaterals of CA3 pyramidal neurons of about 0.5 m/s was assumed and a propagation of a 'locally synchronized discharge' in a two-dimensional array of cells with velocity at only 0.1 to 0.2 m/s was found. Both modelling results are well in line with our experimentally obtained propagation velocities of SPWs in the transverse direction in CA3. However, an understanding of the mechanisms that trigger SPW-Rs and mediate their propagation in CA3 microcircuits will need further investigation.

References

Bazelot, M., Teleńczuk, M. T., & Miles, R. (2016). Single CA3 pyramidal cells trigger sharp waves in vitro by exciting interneurones. *The Journal of Physiology*, **594**(10), 2565–2577.

Buhl, D. L., & Buzsáki, G. (2005). Developmental emergence of hippocampal fast-field "ripple" oscillations in the behaving rat pups. *Neuroscience*, **134**(4), 1423–1430.

Buzsáki, G., Lai-Wo S, L., & Vanderwolf, C. H. (1983). Cellular bases of hippocampal EEG in the behaving rat. *Brain Research*, **6**(2), 139–171.

Buzsáki, G. (1986). Hippocampal sharp waves: Their origin and significance. *Brain Research*, **398**(2), 242–252.

Buzsáki, G. (1989). Two-stage model of memory trace formation: A role for "noisy" brain states. *Neuroscience*, **31**(3), 551–570.

Buzsáki, G. (2015). Hippocampal sharp wave-ripple: A cognitive biomarker for episodic memory and planning. *Hippocampus*, **25**(10), 1073–1188.

Buzsáki, G., Horváth, Z., Urioste, R., Hetke, J., & Wise, K. (1992). High-frequency network oscillation in the hippocampus. *Science*, **256**(5059), 1025–1027.

Çalışkan, G., Demiray, Y. E., & Stork, O. (2023). Comparison of three common inbred mouse strains reveals substantial differences in hippocampal GABAergic interneuron populations and in vitro network oscillations. *European Journal of Neuroscience*, **58**(6), 3383–3401.

Chiovini, B., Turi, G. F., Katona, G., Kaszás, A., Pálfi, D., Maák, P., Szalay, G., Szabó, M. F., Szabó, G., Szadai, Z., Káli, S., & Rózsa, B. (2014). Dendritic spikes induce ripples in parvalbumin interneurons during hippocampal sharp waves. *Neuron*, **82**(4), 908–924.

Chrobak, J. J., & Buzsáki, G. (1996). High-frequency oscillations in the output networks of the hippocampal-entorhinal axis of the freely behaving rat. *The Journal of Neuroscience*, **16**(9), 3056–3066.

Csicsvari, J., Hirase, H., Czurkó, A., Mamiya, A., & Buzsáki, G. (1999a). Oscillatory coupling of hippocampal pyramidal cells and interneurons in the behaving rat. *The Journal of Neuroscience*, **19**(1), 274–287.

Csicsvari, T., Hirase, H., Czurkó, A., Mamiya, A., & Buzsáki, G. (1999b). Fast network oscillations in the hippocampal CA1 region of the behaving rat. *The Journal of Neuroscience*, **19**(16), RC20–RC20.

Csicsvari, J., Hirase, H., Mamiya, A., & Buzsáki, G. (2000). Ensemble patterns of hippocampal CA3-CA1 neurons during sharp wave-associated population events. *Neuron*, **28**(2), 585–594.

De Filippo, R., & Schmitz, D. (2023). Differential ripple propagation along the hippocampal longitudinal axis. *eLife*, **12**, e85488.

Donoso, J. R., Schmitz, D., Maier, N., & Kempter, R. (2018). Hippocampal ripple oscillations and inhibition-first network models: Frequency dynamics and response to GABA modulators. *The Journal of Neuroscience*, **38**(12), 3124–3146.

Egert, U., Okujeni, S., Nisch, W., Boven, K. H., Rudorf, R., Gottschlich, N., & Stett, A. (2005). Perforated microelectrode arrays optimize oxygen availability and signal-to-noise ratio in brain slice recordings 5th International Meeting on Substrate-integrated Micro Electrode Arrays, Freiburg.

Ego-Stengel, V., & Wilson, M. A. (2010). Disruption of ripple-associated hippocampal activity during rest impairs spatial learning in the rat. *Hippocampus*, **20**(1), 1–10.

El Oussini, H., Zhang, C.-L., François, U., Castelli, C., Lampin-Saint-Amaux, A., Lepleux, M., Molle, P., Velez, L., Dejean, C., Lanore, F., Herry, C., Choquet, D., & Humeau, Y. (2023). CA3 hippocampal synaptic plasticity supports ripple physiology during memory consolidation. *Nature Communications*, **14**(1), 8312.

Ellender, T. J., Nissen, W., Colgin, L. L., Mann, E. O., & Paulsen, O. (2010). Priming of hippocampal population bursts by individual perisomatic- targeting interneurons. *The Journal of Neuroscience*, **30**(17), 5979–5991.

English, D. F., Peyrache, A., Stark, E., Roux, L., Vallentin, D., Long, M. A., & Buzsáki, G. (2014). Excitation and inhibition compete to control spiking during hippocampal ripples: Intracellular study in behaving mice. *The Journal of Neuroscience*, **34**(49), 16509-16517.

Evangelista, R., Cano, G., Cooper, C., Schmitz, D., Maier, N., & Kempter, R. (2020). Generation of sharp wave-ripple events by disinhibition. *The Journal of Neuroscience*, **40**(41), 7811–7836.

Fernández-Ruiz, A., Oliva, A., Fermino De Oliveira, E., Rocha-Almeida, F., Tingley, D., & Buzsáki, G. (2019). Long-duration hippocampal sharp wave ripples improve memory. *Science*, **364**(6445), 1082–1086.

Franklin, K. B. J., & Paxinos, G. (2007). *The mouse brain in stereotaxic coordinates* (3rd ed.). Elsevier.

Girardeau, G., Benchenane, K., Wiener, S. I., Buzsáki, G., & Zugaro, M. B. (2009). Selective suppression of hippocampal ripples impairs spatial memory. *Nature Neuroscience*, **12**(10), 1222–1223.

Hájos, N., Karlócai, M. R., Németh, B., Ulbert, I., Monyer, H., Szabó, G., Erdélyi, F., Freund, T. F., & Gulyás, A. I. (2013). Input-output features of anatomically identified CA3 neurons during hippocampal sharp wave/ripple oscillation in vitro. *The Journal of Neuroscience*, **33**(28), 11677–11691.

Ho, J., Tumkaya, T., Aryal, S., Choi, H., & Claridge-Chang, A. (2019). Moving beyond P values: Data analysis with estimation graphics. *Nature Methods*, **16**(7), 565–566.

Imbrosci, B., Nitzan, N., McKenzie, S., Donoso, J. R., Swaminathan, A., Böhm, C., Maier, N., & Schmitz, D. (2021). Subiculum as a generator of sharp Wave-Ripples in the rodent hippocampus. *Cell Reports*, **35**(3), 109021.

Ishizuka, N., Weber, J., & Amaral, D. G. (1990). Organization of intrahippocampal projections originating from CA3 pyramidal cells in the rat. *Journal of Comparative Neurology*, **295**(4), 580–623.

Jadhav, S. P., Kemere, C., German, P. W., & Frank, L. M. (2012). Awake hippocampal sharp-wave ripples support spatial memory. *Science*, **336**(6087), 1454–1458.

Jiang, H., Liu, S., Geng, X., Caccavano, A., Conant, K., Vicini, S., & Wu, J. (2018). Pacing hippocampal sharp-wave ripples with weak electric stimulation. *Frontiers in Neuroscience*, **12**, 164.

Kajikawa, K., Hulse, B. K., Siapas, A. G., & Lubenov, E. V. (2022). UP-DOWN states and ripples differentially modulate membrane potential dynamics across DG, CA3, and CA1 in awake mice. *eLife*, **11**, e69596.

Kanak, D. J., Rose, G. M., Zaveri, H. P., & Patrylo, P. R. (2013). Altered network timing in the CA3CA1 circuit of hippocampal slices from aged mice. *PLoS ONE*, **8**(4), e61364.

Khazipov, R., Khalilov, I., Tyzio, R., Morozova, E., Ben-Ari, Y., & Holmes, G. L. (2004). Developmental changes in GABAergic actions and seizure susceptibility in the rat hippocampus. *European Journal of Neuroscience*, **19**(3), 590–600.

King, C., Henze, D. A., Leinekugel, X., & Buzsáki, G. (1999). Hebbian modification of a hippocampal population pattern in the rat. *The Journal of Physiology*, **521**(1), 159–167.

Kirov, S. A., Petrak, L. J., Fiala, J. C., & Harris, K. M. (2004). Dendritic spines disappear with chilling but proliferate excessively upon rewarming of mature hippocampus. *Neuroscience*, **127**(1), 69–80.

Ko, T.-W., & Ermentrout, G. B. (2007). Effects of axonal time delay on synchronization and wave formation in sparsely coupled neuronal oscillators. *Physical Review E*, **76**(5), 056206.

Kubota, D., Colgin, L. L., Casale, M., Brucher, F. A., & Lynch, G. (2003). Endogenous waves in hippocampal slices. *Journal of Neurophysiology*, **89**(1), 81–89.

Kudrimoti, H. S., Barnes, C. A., & McNaughton, B. L. (1999). Reactivation of hippocampal cell assemblies: Effects of behavioral state, experience, and EEG dynamics. *The Journal of Neuroscience*, **19**(10), 4090–4101.

Lee, A. K., & Wilson, M. A. (2002). Memory of sequential experience in the hippocampus during slow wave sleep. *Neuron*, **36**(6), 1183–1194.

Li, X.-G., Somogyi, P., Ylinen, A., & Buzsáki, G. (1994). The hippocampal CA3 network: An in vivo intracellular labeling study. *Journal of Comparative Neurology*, **339**(2), 181–208.

Lorente de Nò, R. (1934). Studies on the structure of the cerebral cortex II. Continuation of the study of the ammonic system. *Journal für Psychologie und Neurologie*, **46**, 113–177.

Maier, N., Güldenagel, M., Söhl, G., Siegmund, H., Willecke, K., & Draguhn, A. (2002). Reduction of high-frequency network oscillations (ripples) and pathological network discharges in hippocampal slices from connexin 36-deficient mice. *The Journal of Physiology*, **541**(2), 521–528.

Maier, N., Morris, G., Johenning, F. W., & Schmitz, D. (2009). An approach for reliably investigating hippocampal sharp wave-ripples in vitro. *PLoS ONE*, **4**(9), e6925.

Maier, N., Nimmrich, V., & Draguhn, A. (2003). Cellular and network mechanisms underlying spontaneous sharp wave–ripple complexes in mouse hippocampal slices. *The Journal of Physiology*, **550**(3), 873–887.

Maier, N., Tejero-Cantero, Á., Dorrn, A. L., Winterer, J., Beed, P. S., Morris, G., Kempter, R., Poulet, J. F. A., Leibold, C., & Schmitz, D. (2011). Coherent phasic excitation during hippocampal ripples. *Neuron*, **72**(1), 137–152.

Meeks, J. P., & Mennerick, S. (2007). Action potential initiation and propagation in CA3 pyramidal axons. *Journal of Neurophysiology*, **97**(5), 3460–3472.

Miles, R., Traub, R. D., & Wong, R. K. (1988). Spread of synchronous firing in longitudinal slices from the CA3 region of the hippocampus. *Journal of Neurophysiology*, **60**(4), 1481–1496.

Monier, C., Fournier, J., & Frégnac, Y. (2008). In vitro and in vivo measures of evoked excitatory and inhibitory conductance dynamics in sensory cortices. *Journal of Neuroscience Methods*, **169**(2), 323–365.

Moradi-Chameh, H., Peng, J., Wu, C., & Zhang, L. (2014). Intracellular activities related to *in vitro* hippocampal sharp waves are altered in CA3 pyramidal neurons of aged mice. *Neuroscience*, **277**, 474–485.

Muller, L., Chavane, F., Reynolds, J., & Sejnowski, T. J. (2018). Cortical travelling waves: Mechanisms and computational principles. *Nature Reviews Neuroscience*, **19**(5), 255–268.

Nádasdy, Z., Hirase, H., Czurkó, A., Csicsvari, J., & Buzsáki, G. (1999). Replay and time compression of recurring spike sequences in the hippocampus. *The Journal of Neuroscience*, **19**(21), 9497–9507.

Nitzan, N., Swanson, R., Schmitz, D., & Buzsáki, G. (2022). Brain-wide interactions during hippocampal sharp wave ripples. *Proceedings of the National Academy of Sciences*, **119**(20), e2200931119.

Norimoto, H., Makino, K., Gao, M., Shikano, Y., Okamoto, K., Ishikawa, T., Sasaki, T., Hioki, H., Fujisawa, S., & Ikegaya, Y. (2018). Hippocampal ripples down-regulate synapses. *Science*, **359**(6383), 1524–1527.

Oliva, A., Fernández-Ruiz, A., Buzsáki, G., & Berényi, A. (2016). Role of hippocampal CA2 region in triggering sharp-wave ripples. *Neuron*, **91**(6), 1342–1355.

Papatheodoropoulos, C., & Kostopoulos, G. (2002). Spontaneous GABAA-dependent synchronous periodic activity in adult rat ventral hippocampal slices. *Neuroscience Letters*, **319**(1), 17–20.

Patel, J., Schomburg, E. W., Berényi, A., Fujisawa, S., & Buzsáki, G. (2013). Local generation and propagation of ripples along the septotemporal axis of the hippocampus. *The Journal of Neuroscience*, **33**(43), 17029–17041.

Peng, Y., Mittermaier, F. X., Planert, H., Schneider, U. C., Alle, H., & Geiger, J. R. P. (2019). High-throughput micro-circuit analysis of individual human brains through next-generation multineuron patch-clamp. *eLife*, **8**, e48178.

Preibisch, S., Saalfeld, S., & Tomancak, P. (2009). Globally optimal stitching of tiled 3D microscopic image acquisitions. *Bioinformatics*, **25**(11), 1463–1465.

Ramirez-Villegas, J. F., Logothetis, N. K., & Besserve, M. (2015). Diversity of sharp-wave–ripple LFP signatures reveals differentiated brain-wide dynamical events. *Proceedings of the National Academy of Sciences*, **112**(46), E6379–E6387.

Sadowski, J. H. L. P., Jones, M. W., & Mellor, J. R. (2016). Sharp-Wave ripples orchestrate the induction of synaptic plasticity during reactivation of place cell firing patterns in the hippocampus. *Cell Reports*, **14**(8), 1916–1929,

Sammons, R. P., Vezir, M., Moreno-Velasquez, L., Cano, G., Orlando, M., Sievers, M., Grasso, E., Metodieva, V. D., Kempter, R., Schmidt, H., & Schmitz, D. (2024). Structure and function of the hippocampal CA3 module. *Proceedings of the National Academy of Sciences*, **121**(6), e2312281120.

Schlingloff, D., Káli, S., Freund, T. F., Hájos, N., & Gulyás, A. I. (2014). Mechanisms of sharp wave initiation and ripple generation. *The Journal of Neuroscience*, **34**(34), 11385–11398.

Schneiderman, J. H. (1986). Low concentrations of penicillin reveal rhythmic, synchronous synaptic potentials in hippocampal slice. *Brain Research*, **398**(2), 231–241.

Simmonet, J., Richevaux, L., & Fricker, D. (2021). Single or double patch-clamp recordings in ex vivo slice preparation: Functional connectivity, synapse dynamics, and optogenetics. *Patch clamp electrophysiology. Methods and protocols* (Vol., **2188**, pp. 285–309). In M. Dallas & D. Bell (Eds.). Humana.

Soleng, A. F., Raastad, M., & Andersen, P. (2003). Conduction latency along CA3 hippocampal axons from rat. *Hippocampus*, **13**(8), 953–961.

Stark, E., Roux, L., Eichler, R., Senzai, Y., Royer, S., & Buzsáki, G. (2014). Pyramidal cell-interneuron interactions underlie hippocampal ripple oscillations. *Neuron*, **83**(2), 467–480.

Sullivan, D., Csicsvari, J., Mizuseki, K., Montgomery, S., Diba, K., & Buzsáki, G. (2011). Relationships between hippocampal sharp waves, ripples, and fast gamma oscillation: Influence of dentate and entorhinal cortical activity. *Journal of Neuroscience*, **31**(23), 8605–8616.

Swaminathan, A., Wichert, I., Schmitz, D., & Maier, N. (2018). Involvement of mossy cells in sharp wave-ripple activity in vitro. *Cell Reports*, **23**(9), 2541–2549.

Taxidis, J., Coombes, S., Mason, R., & Owen, M. R. (2012). Modeling sharp wave-ripple complexes through a CA3-CA1 network model with chemical synapses. *Hippocampus*, **22**(5), 995–1017.

Tellinghuisen, J. (2020). Least squares methods for treating problems with uncertainty in x and y. *Analytical Chemistry*, **92**(16), 10863–10871.

Traub, R. D., Miles, R., & Wong, R. K. S. (1989). Model of the origin of rhythmic population oscillations in the hippocampal slice. *Science*, **243**(4896), 1319–1325.

Wilson, M. A., & McNaughton, B. L. (1994). Reactivation of hippocampal ensemble memories during sleep. *Science*, **265**(5172), 676–679.

Wong, R. K., & Traub, R. D. (1983). Synchronized burst discharge in disinhibited hippocampal slice. I. Initiation in CA2-CA3 region. *Journal of Neurophysiology*, **49**(2), 442–458.

Wong, T., Zhang, X. L., Nassiri Asl, M., Wu, C. P., Carlen, P. L., & Zhang, L. (2005). Postnatal development of intrinsic GABAergic rhythms in mouse hippocampus. *Neuroscience*, **134**(1), 107–120.

Yamamoto, J., & Tonegawa, S. (2017). Direct medial entorhinal cortex input to hippocampal CA1 is crucial for extended quiet awake replay. *Neuron*, **96**(1), 217–227.e4.

Zarnadze, S., Bäuerle, P., Santos-Torres, J., Böhm, C., Schmitz, D., Geiger, J. R.P., Dugladze, T., & Gloveli, T. (2016). Cell-specific synaptic plasticity induced by network oscillations. *eLife*, **5**, 1–16.

Zutshi, I., & Buzsáki, G. (2023). Hippocampal sharp-wave ripples and their spike assembly content are regulated by the medial entorhinal cortex. *Current Biology*, **33**(17), 3648–3659.e4.

Additional information

Data availability statement

The data that support the findings of this study are available from the corresponding author upon reasonable request.

Supporting information

Additional supporting information can be found online in the Supporting Information section at the end of the HTML view of the article. Supporting information files available:

Peer Review History